**FACULTY
OF MATHEMATICS
AND PHYSICS**
Charles University

MASTER THESIS

Adam Greš

Experimental study of the deformation mechanisms in cobalt by the advanced in-situ techniques

Department of Physics of Materials

Supervisor of the master thesis: RNDr. Ing. Michal Knapek, Ph.D.

Study programme: Physics

Study branch: Physics of Condensed Matter and Materials

Prague 2023

I declare that I carried out this master thesis independently, and only with the cited sources, literature and other professional sources. It has not been used to obtain another or the same degree.

I understand that my work relates to the rights and obligations under the Act No. 121/2000 Sb., the Copyright Act, as amended, in particular the fact that the Charles University has the right to conclude a license agreement on the use of this work as a school work pursuant to Section 60 subsection 1 of the Copyright Act.

In . . . . date . . . .
                                                                Author's signature

i

Title: Experimental study of the deformation mechanisms in cobalt by the advanced in-situ techniques

Author: Adam Greš

Department: Department of Physics of Materials

Supervisor: RNDr. Ing. Michal Knapek, Ph.D., Department of Physics of Materials

Abstract: The behaviour of pure polycrystalline cobalt in compressive deformation is influenced by the presence of high temperature fcc phase. To investigate this influence samples are prepared using annealing at different temperatures (600 °C-1100 °C) with $\approx$ 6-10% of residual fcc phase. Additional sets of samples are also subjected to thermal cycling around the phase transformation temperature for ten or twenty cycles with the goal of stabilising the microstructure and creating material with no fcc fraction. Samples are tested in compression and a decrease in ductility and strength is observed after the the fcc phase is removed using thermal cycling. The interrupted deformation experiment shows that the transformation is rather sluggish and the main contribution of fcc grains to deformation is their ability to accommodate shape change. The presence of 71° boundaries also suggests that the transformation is not fully stabilised and further thermal cycling could lead to further evolution of microstructure. Additionally the slow transformation does not seem to produce detectable acoustic emission (AE) signal. The energies of AE events (recorded mostly around the yield point) follow a power law distribution. This is in line with recent investigations of the collective nature of dislocation motion and the avalanche-like behaviour of dislocation ensembles.

Keywords: cobalt; deformation; acoustic emission; in-situ characterisation; collective dislocation motion

Contents

Introduction

The elementary principle of plastic deformation is the creation and motion or propagation of crystal lattice defects. The deformation mechanisms may include dislocations, stress induced twinning and martensitic transformation, and others. The nature of these effects and their motion or propagation is inherently heterogeneous and discontinuous. For example dislocations move in increments of the atomic spacing of a given material. Yet the deformation observed on a macroscopic scale is continuous exhibiting a smooth deformation curve, aside from cases of plastic instabilities (Lüders bands, Portevin-Le Châtelier effect). Macroscopic deformation is a combination of a very large number of defects and their motion, the dislocation density can reach the order of magnitude $\sim 10^{10}$ cm^{-2} or up to $\sim 10^{16}$ cm^{-2} in heavily deformed materials [1]. It was though that together microscopic defects average out to create macroscopically smooth and continuous deformation. This approach considers interaction between dislocations to be negligible and the contributions of defects independent of each other. This is inconsistent with microscale observations, that have shown dislocation organising into structures, driven by inter-dislocation interactions [2, 3]. Further research showed that between macro and microscale, in the mesoscale region (distances around the magnitude of μm), plastic deformation is accommodated by cooperative motion of large ensembles of crystal defects [4, 5]. This motion has a avalanche-like character where the distribution of the sizes of avalanches usually follows a power law [6]. The dislocation avalanches exhibiting a scale free behaviour and their sizes following a power law distribution point towards the presence of self-organized criticality (SOC) in the system [7], an idea based on fractal behaviour arising from interactions within dynamic systems.

Metals with a hexagonal close-packed (hcp) crystal structure find many applications as engineering materials in transportation and aerospace [8, 9, 10], biomaterials for implants [11, 12, 13] or as nanomaterials [14, 15]. Success of these applications depends on a deeper understanding of the mechanical behaviour of these materials and how deformation is accommodated by the deformation mechanisms present depending on microstructure. This subject of research is made more complex by the unique mechanical properties of hcp metals such as the low number of independent slip systems and subsequent frequent activation of twinning as an additional deformation mechanism. Pure cobalt is of particular interest as it features an almost ideal c/a ratio, low stacking fault energy and a significantly higher melting point compared to Mg, an hcp metal with similar c/a ratio [16, 17]. Critical to the plastic behaviour of pure cobalt is the presence of high temperature martensitic transformation. Upon heating at around the temperature of $673\,\mathrm{K}$ [17] the low temperature hcp phase transforms into a high temperature face centered cubic (fcc) phase. Upon cooling after any high temperature processing some of the fcc phase remains in the hcp material and does further influence its deformation behaviour [18]. How this transformation and the presence of fcc grains influences deformation is not yet fully understood. Additionally studying the collective defect motion a propagation phenomena in this complex situation can provide a new perspective on how this crystal defect behaviour manifests.

Motivation and Aim

The existing research on cobalt is rather limited. Some studies are quite old a thus do not utilise more modern techniques especially in investigation of microstructure [16, 19, 20]. Other more recent studies focus on thin films [21], nanostructured materials [22, 23, 24] or deformation only in tension [20, 25, 26, 27]. Also to the knowledge of the author there is not any work that presents observations of statistical distributions of the magnitudes of elementary plastic events in deformation of pure cobalt.

- The aim of this work is to expand this body of work with new experimental insight based on modern techniques such as electron backscatter diffraction (EBSD) and AE on polycrystalline samples that are observed during compressive deformation. Thus advancing the physical understanding of deformation processes that contribute to plastic deformation in cobalt.

- Additional goal is to test the AE data for power law distribution and confirm whether cobalt fits within the observation made previously with this developing technique. Of special interest is if the observed distributions change depending on the presence of fcc phase.

- To obtain samples with different fcc fractions, thermal processing including annealing and thermal cycling will be used. This work also aims at studying the microstructure produced by these techniques and their effectiveness in engineering a desired state in the material.

1. Theoretical Background

1.1 Plastic deformation of hexagonal metals

The hcp crystal structure is one of the two structures derived from the closest packing of spheres in three dimensions, the other being the fcc structure. Both of these structures are made from planes of closest packed spheres, where each sphere is surrounded by six other spheres. These planes are then stacked with spheres of one plane fitting above and bellow the void between spheres of the adjacent planes. There are two different positions such a plane can be placed in, with respect to an other plane. These are commonly denoted B and C, with A denoting the reference plane. From this come two ways to periodically arrange these closely packed planes in space - ABABAB... and ABCABC... respectively. The ABABAB... arrangement results in an hcp structure with a hexagonal symmetry and the ABCABC... arrangement results in an fcc structure with cubic symmetry. The unit cell of the hcp structure is defined by two lattice constants commonly denoted a and c. In the ideal scenario following the closest packed spheres the ratio of these two constants is $c/a = \sqrt{8/3}$. In real hcp materials, this ratio deviates from the ideal.

When a metal is subjected to stress beyond the yield point σ_y, the material starts to permanently change its shape. The observed macroscopic changes are the collected result of microscopic crystallographic changes. One of the main mechanisms of these changes is slip. During slip parts of the crystal lattice move with respect to each other, which is the result of dislocations moving on a given slip plane along a slip direction. Generally the most active slip system is the one following the most closely packed plane and the most closely packed direction on this plane. Another mechanism, common in hcp metals is twinning. Twinning is a plastic deformation mechanism which causes a part of the crystal lattice to transform into a lattice mirrored with respect to the twinning plane. Unlike slip, twinning displaces larger number of atoms simultaneously by a fraction of atomic spacing [28].

In pure metals with hcp crystal structure the main slip modes are basal $\{0001\}\langle11\bar{2}0\rangle$, prismatic $\{10\bar{1}0\}\langle11\bar{2}0\rangle$, first pyramidal $\{\bar{1}0\bar{1}1\}\langle11\bar{2}0\rangle$ and second pyramidal $\{11\bar{2}2\}\langle11\bar{2}3\rangle$ [16]. These slip systems are illustrated in Figure 1.1. Activation of slip modes depends on the critical resolved shear stress (CRSS), which is a constant for a given material. Resolved shear stress is an applied stress multiplied by the Schmid factor (SF) m,

$$m = \cos\varphi\cos\lambda, \tag{1.1}$$

where φ is the angle between the applied uniaxial stress axis and the slip plane normal and λ is the angle between the applied uniaxial stress axis and the slip direction [29]. A slip system is activated once the resolved shear stress reaches above the CRSS value. The symmetry of the hcp structure allows only for a limited number of independent slip systems, compared to fcc metals for example. Due to the symmetry present, basal and prismatic system both present only three independent slip systems. For a homogeneous deformation of a polycrystalline material another system incorporating the $\langle c\rangle$ direction is necessary [30, 31]. The

4

second pyramidal slip system can play this role, but in most cases its CRSS is too large for it to be effectively activated. This leads to the activation of twinning. The $\{10\bar{1}2\}$ twinning mode (Fig. 1.2) has the lowest CRSS in all hcp metals and is the most commonly activated one [16, 32]. Unlike slip, the activation of twinning depends on the loading direction. The $\{10\bar{1}2\}$ twinning mode is also known as extension twin since it accommodates extension in the c direction. Because of this the $\{10\bar{1}2\}$ twinning will be likely to activate in the case of tensile load along the c direction or compressive load perpendicular to the c direction. Other twinning modes less frequently observed in hcp metals are $\{10\bar{1}1\}$ and $\{10\bar{1}3\}$ twins in magnesium and cobalt [27, 33, 34] or $\{11\bar{2}1\}$ and $\{11\bar{2}2\}$ twins in titanium and zirconium [35, 36, 37].

| (a) Basal | (b) Prismatic | (c) First pyramidal | (d) Second Pyramidal |
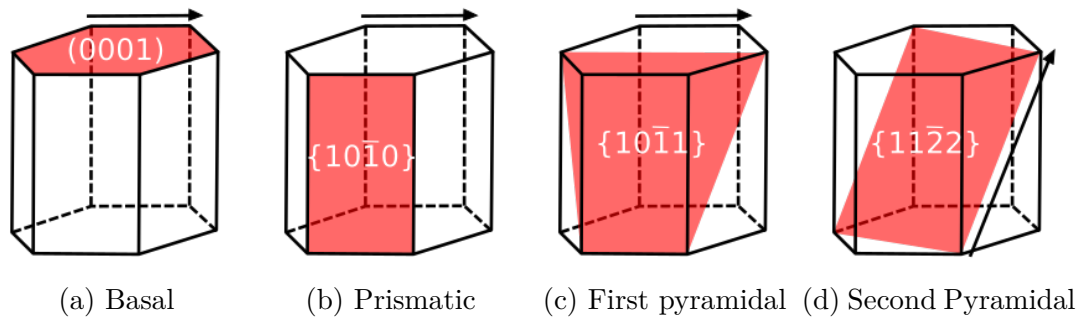
Figure 1.1: Illustration of slip modes observed in metals with hcp structure. The slip plane is highlighted in red with an arrow showing the slip direction.
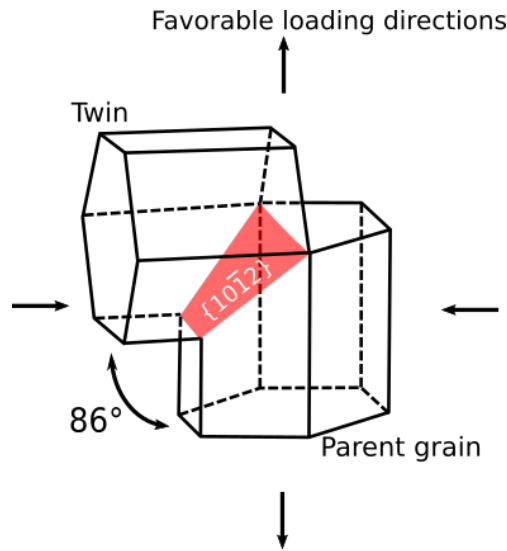

Figure 1.2: The geometric relation of the crystal lattice in parent and twinned grain of the $\{10\bar{1}2\}$ twinning mode. Added arrows illustrate the favourable loading directions – tensile along c axis and compressive along the $\langle 11\bar{2}0 \rangle$ direction.

Metals with hcp structure are often divided into two groups by their c/a ratio. Metals with c/a close to or higher than the ideal $\sqrt{8/3} \approx 1.633$ include Cd, Zn, and Mg. These metals share a lower melting point (650 °C for Mg, or lower) and their primary slip mode is basal, since the basal plane is the most closely packed plane in this case. The other group are metals with c/a lower than the ideal.

These are Zr, Ti and Be and their melting points are higher (1277 °C for Be or higher). In this case the basal plane is not the most closely packed and therefore the main slip system is prismatic [32], with the exception of Be [38]. Cobalt is an exception to this division. It has c/a ratio very close to Mg. On the other hand cobalt exhibits a higher melting point of 1495 °C and a high temperature allotropic transformation like the elements with c/a ratio bellow ideal [16].

1.2   Cobalt

Cobalt possesses certain characteristics which make it somewhat stand out among hcp metals. The c/a ratio of pure cobalt is ≈ 1.623 which is very close to the ideal value of ≈ 1.633. Compared to magnesium with almost identical c/a ratio cobalt has significantly higher melting temperature and lower stacking fault energy. The stacking fault energy in cobalt is $\approx 31 \, \mathrm{mJ \, m^{-2}}$ [17]. This is fairly low for a hcp metal, for example the stacking fault energy of magnesium is $\approx 125 \, \mathrm{mJ \, m^{-2}}$ [39]. This stacking fault energy causes dislocations in the close packed basal plane to be extended and the distance between the partial dislocations to be long. The result is a low probability of cross-slip into other slip planes. This contributes to a lack of non-basal slip activity, which leads to more twinning activity.

Pure cobalt exhibits a martensitic phase transformation between a fcc high temperature phase and a hcp low temperature phase. Equilibrium temperature of this transformation is approximately 673 K [17]. This transformation stands out among hcp metals as other hcp metals have either no high temperature phase or body centered cubic (bcc) high temperature phase, making this transformation a unique case [16]. The generally accepted theory explaining the mechanism behind this transformation is present in [40]: during cooling the transformation is accommodated by partial dislocations moving across every other closely packed (111) plane in the fcc phase changing the arrangement of the closely packed planes from ABCABC... into the ABABAB... arrangement of closely packed planes of the hcp structure. Figure 1.3 illustrates this process. Associated austenite start temperature A_S can wary between 694 K and 720 K, while martensite start M_S can be between 692 K and 661 K [40]. After cooling some amount of the fcc phase may be retained, the exact amount depends on many factors including thermal history, internal stresses of the material and purity. It has been shown that the fraction of fcc phase can be stabilised after thermal cycling around the transformation temperature [41, 42, 43]. This suggests the possibility of manufacturing cobalt with a well defined fraction of fcc phase free of the influence of all the previously mentioned factors. This stabilisation can then progress further. Due to the mechanism of the transformation a single fcc grain has four systems of {111} planes and so four orientations of hcp phase can be created during deformation. It is observed that initially a single fcc grain transforms into multiple grains of hcp with c axes oriented along different $\langle 111 \rangle$ directions of the original grain. After prolonged thermal cycling the transformation eventually develops to a point where each fcc grain transforms into a single hcp grain of a given orientation due to the process show in Figure 1.4 [40, 41, 44].
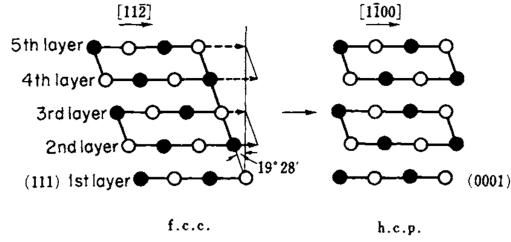
Figure 1.3: Illustration of how the shifting of planes changes the structure of cobalt from fcc to hcp. This shift is accommodated by the dissociation of perfect dislocations in the {111} plane [45].
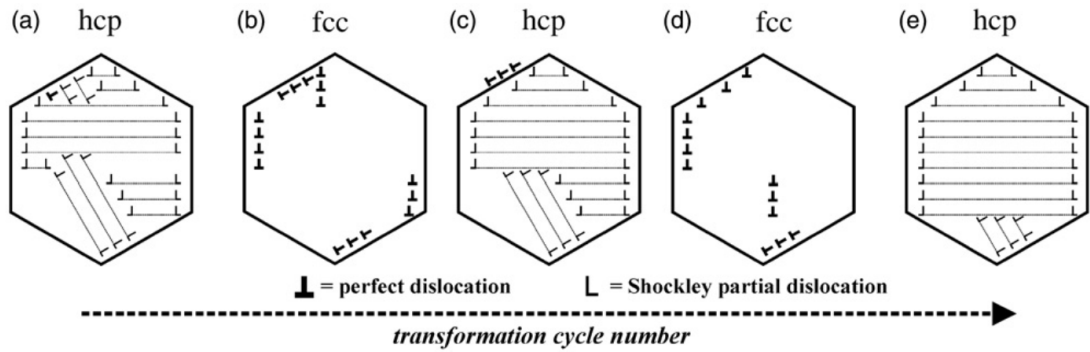

Figure 1.4: Simplified illustration of the process that takes place during thermal cycling. Initially (a) the grain is broken into multiple smaller grains as arrays of dissociating dislocations form in the four different sets of {111} planes. These arrays then grow independently transforming the grain into multiple smaller parts. During thermal cycling (b) and (c) smaller arrays of dislocations are limited in motion or even fully pushed out and incorporated into the grain boundary. With enough cycles (d), (e) the transformation evolves toward ideally only a single stack of dislocations transforming it completely [40].

The main slip system observed in cobalt is the basal slip system. At the same time there seems to be little evidence of any other slip system activating [16, 32]. This might be the combination of the low stacking fault energy in cobalt making cross-slip difficult and the fact that non-basal planes undergo more significant rearrangements during the fcc to hcp transformation, potentially erasing dislocations and dislocation sources on non-basal planes. In cobalt as in other hcp metals the most easily activated twinning mode is extension {10$\bar{1}$2} twin [16, 46]. There is approximately 86° misorientation between the twinned grains of this system and the parent grain. The {10$\bar{1}$1}, {11$\bar{2}$1} and {10$\bar{1}$3} twinning modes have also been reported in cobalt during tension [27, 47]. The {11$\bar{2}$1} twinning mode with approximately 34° misorientation was also observed during compression [46]. The almost complete lack of secondary slip system in cobalt creates a intriguing situation, where most of plastic deformation is accommodated just by one slip system, usually one twinning mode and potentially transformation of any remaining fcc phase. Each grain can then experience a different amount of slip or twinning depending on its orientation in relation to the loading direction. In the case twinning is activated, the new twin grain may be oriented more favourably for basal slip and thus create more opportunities for further deformation.

7

1.3   Compression Testing

During a compression test the deformation behaviour of a sample is evaluated under uniaxial compressive loading. The sample is placed between two pressure plates in a mechanical testing machine and compressed under increasing force as a function of constant-rate platen displacement. During the test the force F and shortening ΔL of the sample are measured. These values are used to determine engineering stress σ and engineering strain ε as:

$$\sigma = \frac{F}{S_0}, \quad \varepsilon = \frac{\Delta L}{L_0}, \tag{1.2}$$

where S_0 represents initial cross section of the sample, L_0 represents initial length of the sample. Plotting σ versus ε results in a engineering stress-strain diagram. Fig. 1.5 illustrates a general shape of a stress-strain curve during a test with a constant strain rate $\dot{\varepsilon}$. The stress-strain relation is linear for small strains, where the deformation is elastic. After exceeding yield stress σ_y the deformation enters the plastic regime. In the plastic regime the stress at first increases with strain until it reaches its maximum value called ultimate compressive strength (UCS). At higher strains the stress decreases with strain until reaching the fracture of the specimen. Since the transition from the elastic to the plastic regime is continuous, yield stress is not uniquely defined. Most common definition of yield stress is $\sigma_{0.2}$, which is the stress, where strain is 0.2 % higher than elastic strain of the given stress.
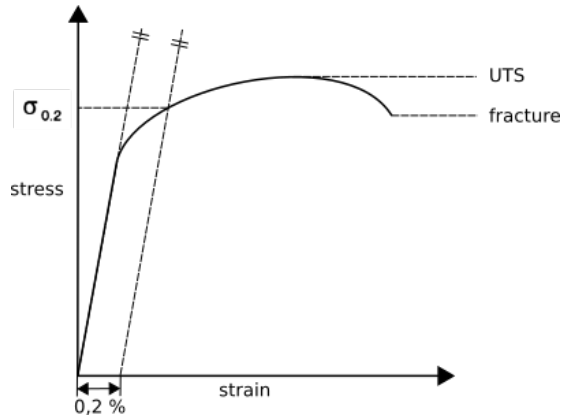
Figure 1.5: Common features of stress-strain curves.

For plastic deformation during which high strains are attained the cross section and the length of the sample differ greatly from the initial values S_0 and L_0. For this reason true strain σ_t and true stress ε_t are defined. True strain ε_t is defined in differential terms as

$$d\varepsilon_t = \frac{dL}{L}, \tag{1.3}$$

where L represents the current length of the sample. The relation between engineering strain ε and true strain ε_t is

$$\varepsilon_t = \int_{L_0}^{L} \frac{dL}{L} = \ln \frac{L}{L_0} = \ln \frac{L_0 - \Delta L}{L_0} = \ln(1 - \varepsilon). \tag{1.4}$$

True stress σ_t is defined as

$$\sigma_t = \frac{F}{S}, \tag{1.5}$$

where S represents the current cross section of the sample. During deformation the volume of the sample remains constant, thus $L_0 \cdot S_0 = L \cdot S$. Therefore,

$$\sigma_t = \frac{F}{S} = \frac{F}{S_0}\frac{S_0}{S} = \sigma\frac{L}{L_0} = \sigma(1-\varepsilon). \tag{1.6}$$

If the focus is on the plastic region of deformation, plastic strain can be used. To determine plastic strain, the elastic modulus $E = \sigma/\varepsilon$ must first be determined by fitting the linear region of elastic deformation. After this for any point on the deformation curve defined by its σ and ε, the plastic strain ε_p is determined as

$$\varepsilon_p = \varepsilon - \frac{\sigma}{E}. \tag{1.7}$$

The same procedure can be used to determine true plastic strain by using the true values of stress and strain.

1.4 Acoustic Emission Technique

The AE technique is a non-destructive in-situ method, which has gained great popularity in the last decades. The AE is elastic energy released during local, irreversible changes in the microstructure of the materials such as those that happen during plastic deformation and phase transformation in metals. This energy travels through the material as an elastic wave. Once this wave reaches surface of a sample its component perpendicular to the sample surface can be detected with a piezoelectric sensor which is in contact with the sample surface. The electric signal from the sensor can then be captured in real time and saved for further study. Measuring AE can thus provide information about the process of mechanical deformation in real time.

To measure AE signal during deformation a sensor is attached to the sample. The signal from the microphone is then amplified in the preamplifier before entering the AE system, which further amplifies the signal, converts from analogue to digital and processes it, before sending the data to a connected PC for further analysis (Fig. 1.6).
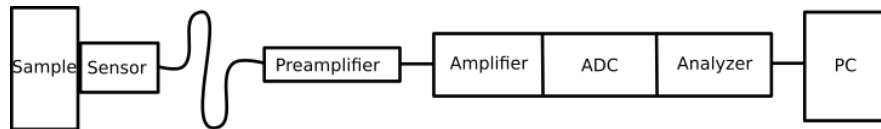
Figure 1.6: Diagram of typical AE measuring equipment.

Two elementary categories of AE signal can be distinguished: continuous and discontinuous. During continuous signal the amplitude of the signal does not fall under a given threshold for a longer period of time. Discontinuous signals are on the other hand bursts well separated in time, often of much higher maximum amplitude and energy. Continuous signal is associated with dislocation glide and stress relaxation [48], but also with friction or machine noise. Discontinuous

signal can be caused by nucleation of twins, crack initiation and propagation and corrosion processes [49]. It has been shown that continuous signal is often a sum of random overlapping pulses [50].

Traditionally AE signal is analysed using a parameter based approach. This approach avoids storing the full record of AE data, by identifying significant AE events and only storing parameters of these events. Figure 1.7 illustrates the commonly used AE event parameters:
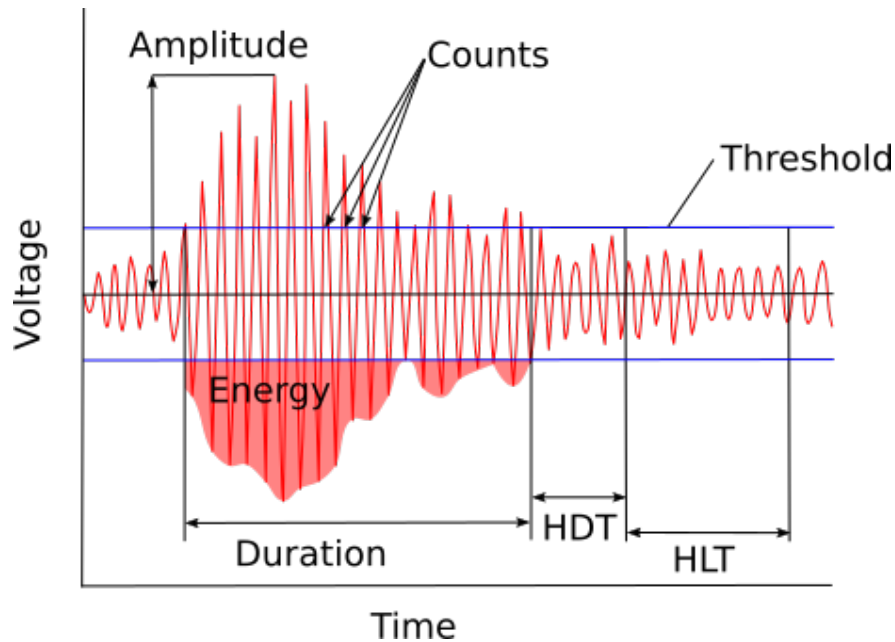

Figure 1.7: Scheme of AE event and its parameters.

These parameters are:

- *Threshold.* When the detected value of voltage goes above the defined threshold, an event starts. This way noise between events is not recorded.

- *Hit definition time (HDT).* End of an event is defined by HDT. Once the detected signal stays under the threshold for the duration of HDT the event is ended.

- *Hit lockout time (HLT).* After the end of an event for the duration of HLT no new event can be triggered. It is sometimes also referred to as *dead time.* This is a measure which prevents the recording of sound reflections.

- *Duration.* Once an event ends, the time from its start to the beginning of HDT is recorded as its duration.

- *Counts.* Refers to the number of times the observed signal crossed the threshold during the duration of an event.

- *Amplitude.* Maximum voltage reached during an event.

- *Energy.* This can be defined in multiple ways. Most common is the area under the amplitude curve of the signal during the duration of an event.

Analysing AE signal using a parameter based approach minimised the amount of stored data. With newer and better AE devices and generally more accessible high capacity data storage it is also possible nowadays to record the raw signal. Such signal can then be analysed again using the parameter based approach later after the experiment, even multiple times. This way it is possible to tune the parameters (threshold, HDT, HLT).

1.5 Power law statistics

Power law distributions are of a great importance as they appear in different phenomena in many different branches of science. A quantity x obeys a power law if its probability distribution is

$$p(x) \propto x^{-\alpha}, \tag{1.8}$$

where α is a constant parameter sometimes referred to as scaling parameter. In practice only the tail of the distribution follows a power law while for x smaller than a $x_{\min}$ it does not apply. It is often preferable to visualise the distribution utilising the complementary cumulative distribution function (CCDF) $P(x)$ defined as $P(x) = \text{probability of}(X \geq x)$ as its visual form is less influenced by fluctuations in the data especially in the tail end of the distribution. In the case of power law, the CCDF is [51]

$$P(x) = \left(\frac{x}{x_{\min}}\right)^{-\alpha+1}. \tag{1.9}$$

While it is possible to find out the α parameter by applying least-squares linear regression to a log-log plot of the probability histogram a more suitable approach is to use maximum likelihood estimators (MLE) method [51]. The MLE for α in the case of n measured points is

$$\alpha_{\mathrm{ML}} = 1 + n \left[\sum_{i=1}^{n} \ln \frac{x_i}{x_{\min}}\right]^{-1}, \tag{1.10}$$

where x_i are observed values of x such that $x_i \geq x_{\min}$ [52]. To fit empirical data with a power law it is also necessary to estimate the $x_{\min}$ parameter. A method proposed in [53] estimates the $\hat{x}_{\min}$ value by Kolmogorov-Smirnov (KS) statistic [54] minimisation. The KS statistic is the maximum distance between the data and the fitted model. For each possible $x_{\min}$ value the KS statistic is calculated and the lowest values is chosen.

Well suited experimental technique to observe the power laws present in plastic deformation is AE. The scale spectrum of crystal defect avalanches that can be observed using AE is very wide and the first ever evidence of this behaviour measured on crystal ice was detected using AE [55]. The power law distributions are found in the distributions of the amplitude of AE events squared as the amplitude squared is proportional to the energy of the event $E \propto A^2$. This is based on the estimate of energy dissipated by a single screw dislocation $E \propto L^2 b^2 v^2$, where L is length of the dislocation, v the average velocity, and b its Burgers vector [56]. At the same time the amplitude of the elastic wave generated

by a dislocation avalanche follows the proportionality $A \propto Lbv$ [57]. Further research showed the presence of power law distributions in a wide variety of materials [6, 58, 59, 60]. The coefficients of the observed distributions seemed to be in the range of $\alpha \approx 1.5 - 1.8$ independent of material or structure, giving rise to a universality conjecture [61]. A change in power law coefficients outside of this range was observed in the case of crystal ice [57, 62, 63] and during plastic instabilities [5, 64, 65].

1.6 SEM and EBSD

Scanning electron microscopy (SEM) is an experimental method utilising a beam of accelerated electrons to scan point by point over the surface of the sample. Electrons that impact the sample interact with the material in an interaction volume bellow the point of impact and then exit the sample. These electrons are then collected to create an image. Figure 1.8 illustrates the basic structure of SEM. Electrons are emitted from a source and accelerated by an electric field and pass through multiple apertures and magnetic lenses to create a uniform focused beam. The interactions between the impacting electrons and the sample cause emission of electrons and photons that are detected in multiple different ways. The two most commonly used modes of observation are secondary electrons (SE) and back-scattered electrons (BSE). SE are electrons that leave an atom in the sample after they receive energy from a beam electron inelastically interacting with the atom. These SE have generally lower energy and can only escape from the region closest to the surface. The SE detector is usually placed to the side of the chamber and attracts these slower electrons using a mesh with positive potential. BSE are beam electrons that are reflected from the sample via elastic scattering and can escape even from deeper regions of the sample. Most BSE will exit the sample moving in a direction close to the reverse of the beam. Because of that detectors of BSE are often a ring around where the beam enters the specimen chamber.
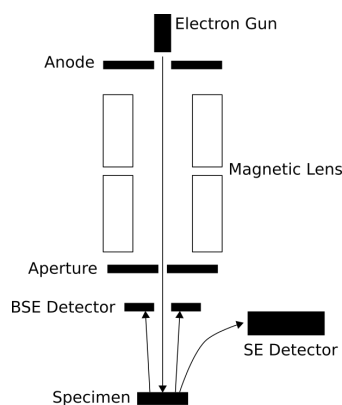
Figure 1.8: Schematic of SEM.

A more advanced SEM technique for studying the crystallographic structure of material is EBSD. To observe EBSD the sample is rotated and the beam reflected from the sample to a phosphorescent screen combined with a low-light camera. Electrons are scattered in different directions with different energies

upon impact. Those that fulfil the condition set by the Bragg's law will then diffract on the crystal's periodic lattice. The cone of diffracted electrons intersects with the screen of the EBSD camera, tracing a hyperbola across the screen, which can be approximated as a straight line. These lines are know as Kikuchi lines. The Kikuchi pattern of lines observed by the EBSD camera can then be further digitally processed and crystallographic orientation for each point can be extracted. This results in an orientation map, where crystallographic orientation is determined for each point/pixel. This can be used to determine grain size, by defining continuous regions of almost identical orientation as grains and determining the distribution of grain sizes represented on the map. Twins can be detected on the map by having the software detect boundaries between grains that fulfil the geometric relations of twin and the parent grain, which are exactly defined for each twinning mode. In the case of dislocations, unlike transmission electron microscopy SEM in general does not have the resolution necessary to detect individual dislocations. But the kernel average misorientation (KAM) technique can be used to infer the density of geometrically necessary dislocations, as it is proportional to local misorientation [66, 67]. KAM of a given point is calculated by determining the misorientation between the point and each adjacent point and these misorientations are then averaged. It is also possible to calculate KAM using second or further neighbours.

2. Materials and Methods

Samples studied in this work were cut from as-drawn pure cobalt. These rods were purchased from Goodfellow Cambridge Ltd. (Huntingron, England). The purity of the material was 99.9 %, with quoted impurities being (in ppm): Fe - 180, Ni - 800, C - 30, S - 150. These rods were 200 mm long and their diameter was 6.35 mm. The initial microstructure before any thermal processing is captured in Figure 2.1. The as-drawn cobalt material has grain size of $\approx 9\,\mu m$, fcc fraction of ≈ 2 %, texture commonly seen in extruded hcp materials [68] as was determined using the methods described further in this chapter. Three sets of six sample types each were cut from these rods, each a cylinder with a height of 9 mm. All samples were annealed using the vertical furnace Nabertherm RHTV 120-600 (Lilienthal, Germany) for 1 h under vacuum and water-quenched. The annealing temperatures were between 600 °C and 1100 °C with 100 °C step and each set contained one sample type per annealing temperature. The second and third sets were further subjected to thermal cycling around the cobalt phase transformation temperature in order to stabilise the transformation as discussed in Section 1.2 and create samples with well defined fcc fraction. The thermal cycling was performed using the Linseis L75 PT vertical thermodilatometer (Selb, Germany), under an Ar atmosphere. One thermal cycle consisted of heating from 300 °C to 550 °C at the rate of $5\,°C\,min^{-1}$ and cooling back to 300 °C at the same rate. The second set of samples was subjected to 10 such cycles, while the third set was subjected to 20 cycles. During cycling thermodilatometry (TD) data was also recorded. For the remainder of this work the following naming scheme will be used for these samples: coxxxx-yyc, where "xxxx" is replaced by the annealing temperature of the sample and "yy" is replaced with the number of cycles. Samples that were not subjected to thermal cycling will just be labelled as "coxxxx". An additional set of samples in the shape of small discs weighting $\approx 30\,mg$ were cut and subjected to differential scanning calorimetry (DSC) under the thermal cycling conditions described above. Figure 2.2 shows the data measured during TD and DSC. It is observed that with increasing number of cycles the heat flow and length change profiles change. This evolution is more pronounced during the first few cycles. With additional cycles the evolution slows down, consistent with the stabilisation of the transformation. The cooling peak in DSC is visibly lower and wider compared to the heating peak. This suggest that the martensitic fcc to hcp transformation is slower compared to the austenitic hcp to fcc transformation.

Microstructure of the samples was investigated using EBSD. Before any SEM observations the samples were prepared by grinding using increasing grit emery papers and polishing using diamond suspensions with decreasing particle sizes down to 1 µm. The final step was ion etching performed using Leica EM RES102 (Leica Mikrosysteme, Wetzlar, Germany). The SEM used for the measurements was ZEISS Auriga Compact FIB-SEM (Jena, Germany), equipped with the EDAX EBSD camera (Berwyn, Pennsylvania, USA). Two sets of measurements were performed. The first consisted of 400×400 µm^2 area maps collected with a step size of 0.4 µm. The purpose of this set of maps was to measure the volume fraction of the residual fcc phase. The second set of EBSD maps was col-
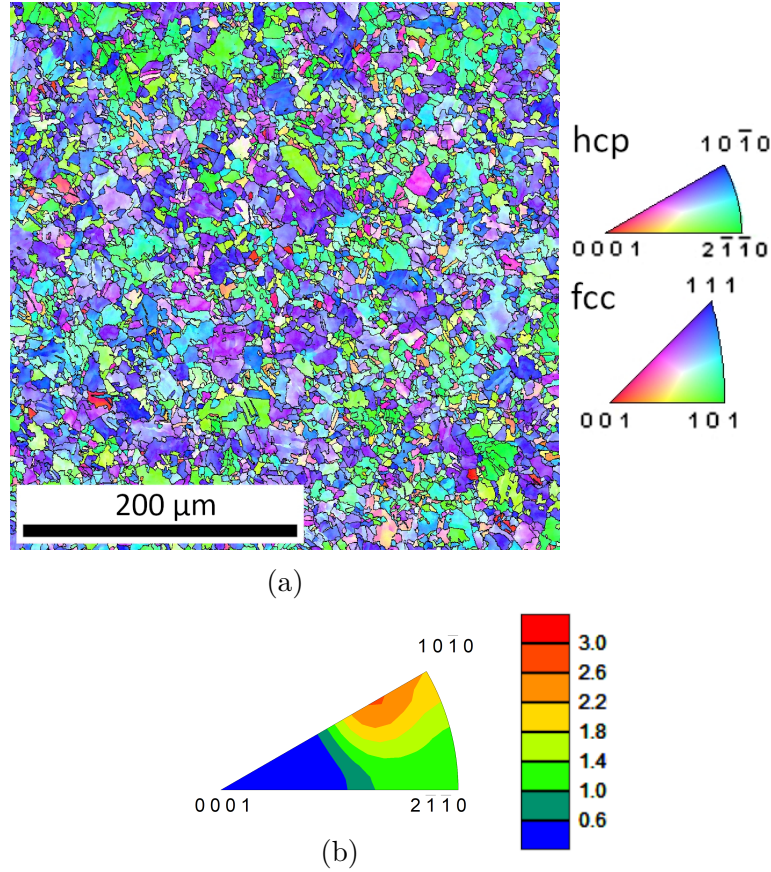
Figure 2.1: Orientation map (a) and inverse pole figure (IPF) (b) of the as-drawn material. The map plane is perpendicular to the drawing direction of the rod (lengthwise along the rod).

lected with area of 1000×2000 µm^2 with step size of 1.5 µm to measure grain size and texture of the hcp phase. The reason behind repeating the measurement with different scan and step size was the difference in grain size as the hcp grains were significantly larger than the fcc grains. The IPFs of selected thermally treated samples are shown in Figure 2.3. The IPFs were generated from the EBSD data using harmonic series expansion up to the rank 16. It can be seen that after annealing at the lowest temperature of 600 °C the initial texture present in the as-drawn material disappears likely due to recrystallization. Further thermal cycling does not create any new considerable texture component either. Thus, all the thermally treated samples exhibit a rather random grain orientation. The EBSD data was further cleaned and processed using the EDAX OIM TSL 7 software. The cleanup consisted of one step of confidence index (CI) standardisation, one step of phase neighbour correlation and one iteration of grain dilatation. For further analysis only points with CI of 0.1 and higher were chosen. For the purpose of both grain size calculation and cleanup, misorientation higher than 15° was considered a grain boundary [69]. Average grain size was weighted by area fraction of the grains. Phase maps were generated automatically by the software by choosing hcp or fcc depending on which fits the observed pattern better.

The compression tests were performed using the Instron 5882 (Northwood, Massachusetts, USA) universal testing machine at room temperature and with
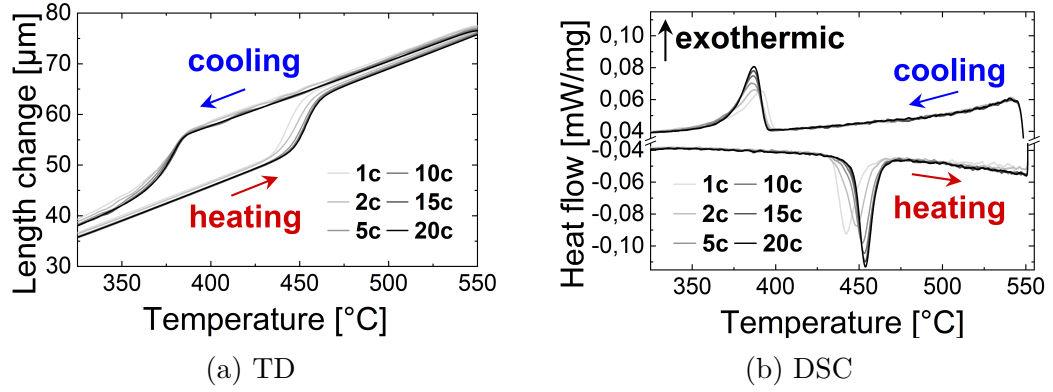
Figure 2.2: The evolution of (a) TD and (b) DSC during thermal cycling. Data captured during selected cycles are shown.

initial strain rate of $\dot{\varepsilon} = 10^{-3}$ s^{-1}. To lower the friction between the sample and the testing machine and prevent barrelling, Apiezon M grease was applied. The machine stiffness was subtracted from measured data before subsequent processing. Several tests were performed to verify the results could be replicated. The systematic error was determined to be 3 %. During deformation AE data were also acquired using the PICO sensor, 2/4/6 - switch selectable preamplifier and the PCI-2 board (Physical Acoustics, New Jersey, USA). The sensor was attached to the specimen holding jaws as close to the sample as possible. The full raw waveform was recorded to allow for more options of further processing. Event detection and parametrization was performed using custom script in MATLAB (The MathWorks, Inc.). For the event detection HDT of 10 µs and HLT of 500 µs were used to optimise the data for probability distribution fitting. The low setting of HDT is set to prevent multiple burst signals combining into a single event. Threshold was set at 0.05 V to prevent background noise and continuous signal to trigger event detection. For the samples co600 – co1000 with lower amplitudes of AE events, the threshold was set lower down to 0.01 V to extract enough events, while still avoiding the lower continuous background observed in these samples. The distributions of amplitudes of AE events have to been shown to be quite robust against the change of these parameters [70]. Fitting of probability distributions with a power law was done using the powerlaw package [71]. This package uses MLE fitting method as described in [51]. The distribution with the fitted function are displayed as CCDF with logarithmic binning.

An additional set of interrupted compression tests combined with EBSD was performed in order to analyse the activity of different deformation mechanisms in relation to the microstructure of selected samples. For the purpose of these test the samples co600, co800, co1100 and co1100-20c were chosen. Three samples were chosen to observe the effect of annealing temperature and the resulting microstructure. The last sample co1100-20c was chosen as a representative of thermally cycled samples. These samples were first prepared for EBSD following the same procedure of EBSD preparation as described above. First an EBSD measurement was performed on the initial undeformed state of each sample. Subsequently a sample was removed from the SEM and placed in the testing machine, deformed to 1 % strain and moved back into the SEM for another EBSD measurement. This process was also repeated for strains of 4 %, 10 %, 20 % and
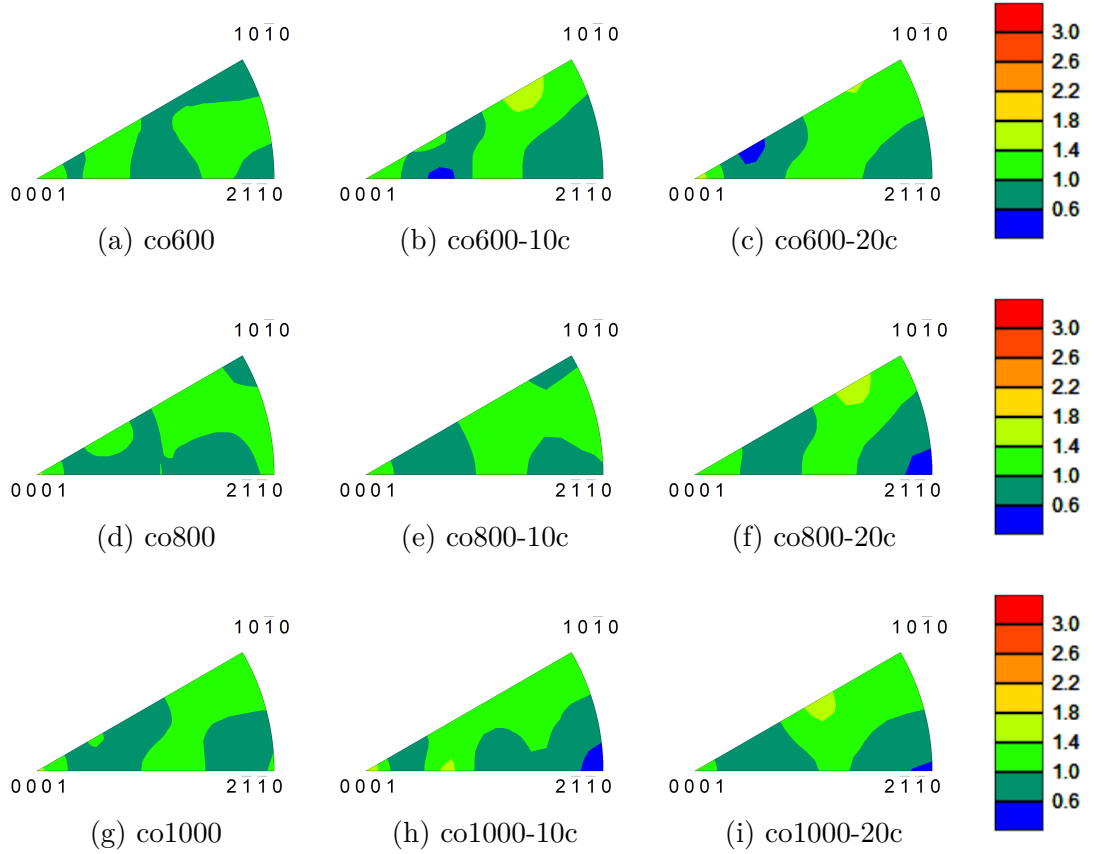
Figure 2.3: Textures of selected samples shown on IPF.

30 %. After the initial measurement, every subsequent EBSD map was taken from the same area on the surface of the sample. All EBSD maps were collected with area of $400 \times 400\ \mu m^2$ and with step size of $0.4\ \mu m$. The EBSD data was further cleaned and processed using the EDAX OIM TSL 7 software. The cleanup consisted of one iteration of NPAR, reindexing points with CI lower than 0.1, one step of CI standardisation and one iteration of grain dilation. Throughout the entire process, misorientation higher than 15° was considered a grain boundary [69]. Only points with CI higher than 0.1 were chosen for further analysis. Data cleaned up using only NPAR were used for the purpose of KAM analysis. KAM analysis was carried out with 5° misorientation between neighbours as the cutoff. This cutoff is implemented to exclude grain boundaries from the KAM calculation.

3. Results

3.1 Sample Characterisation

The effect of thermal preparation including annealing and annealing combined with thermal cycling on the microstructure of the samples was observed using EBSD. The orientation maps and phase map acquired this way are in Figures 3.2 and 3.3 for annealed samples, Figures 3.4 and 3.5 for ten thermal cycles, Figures 3.6 and 3.7 for twenty cycles. From these observations and the additional larger maps the grain size and fraction of the high temperature fcc phase was deduced. The resulting values are listed in Table 3.1. Figure 3.8 illustrates the measured grain size for samples annealed at different temperatures. Without thermal cycling a clear dependence on annealing temperature can be observed together with grain size increase compared to the initial as drawn state. The observed grain size increases from $\approx 22\,\mu m$ for the co600 sample to $\approx 47\,\mu m$ for the co1100 sample. This dependence is still mostly retained after thermal cycling for ten cycles. For this set of samples the grain size is between $\approx 50\,\mu m$ for the co700-10c sample and $\approx 70\,\mu m$ for the co1100-10c sample. The co600-10c is an outlier with grain size of $\approx 31\,\mu m$. After thermal cycling for twenty cycles there is not a strong dependence of grain size on the temperature used during annealing before thermal cycling. The grain size increases compared to the state after ten cycles and is in the range from $\approx 59\,\mu m$ to $\approx 68\,\mu m$. As can be seen in Figure 3.9, after annealing the samples retain between $\approx 6\,\%$ and $\approx 11\,\%$ of residual high temperature fcc phase. There is no clear relationship between the amount of fcc phase and the annealing temperature. After thermal cycling for ten or twenty cycles the amount of fcc phase present in the samples is reduced to $< 1\,\%$ for all samples. The sample co600-10c is, again, an outlier with slightly higher fcc fraction. This seems to indicate that at twenty thermal cycles a well defined microstructure is reliably produced.
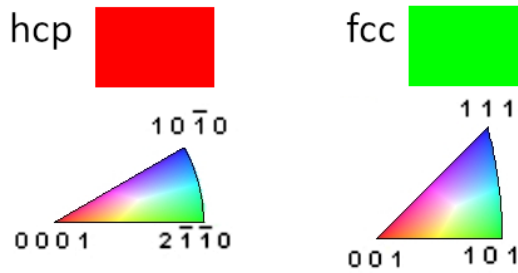
Figure 3.1: A key for the following orientation and phase maps. The map plane in all the EBSD maps in this section is perpendicular to the drawing direction of the rod.
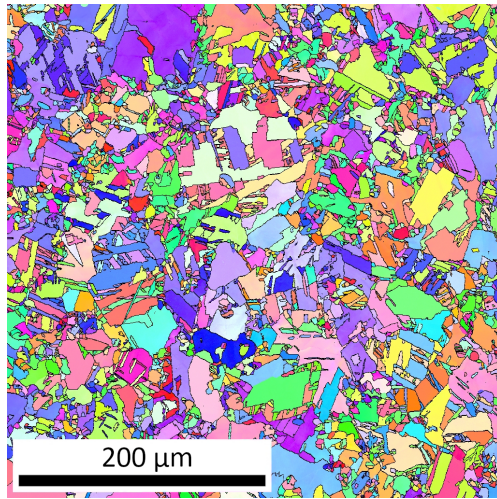
(a) co600
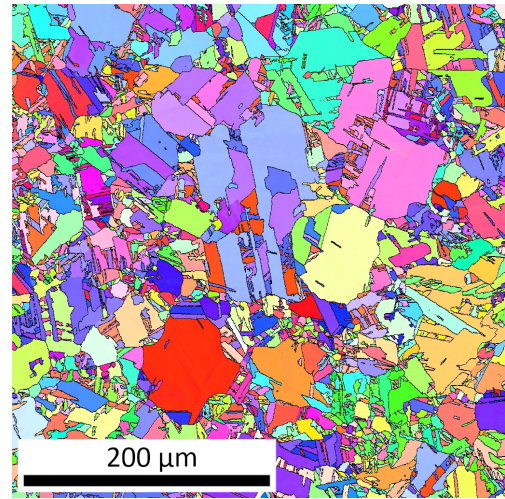
(b) co700
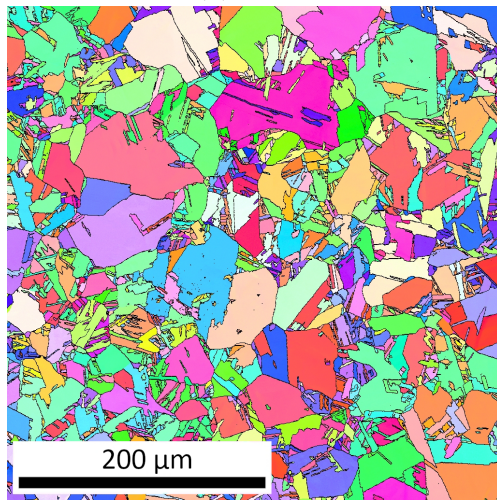
(c) co800
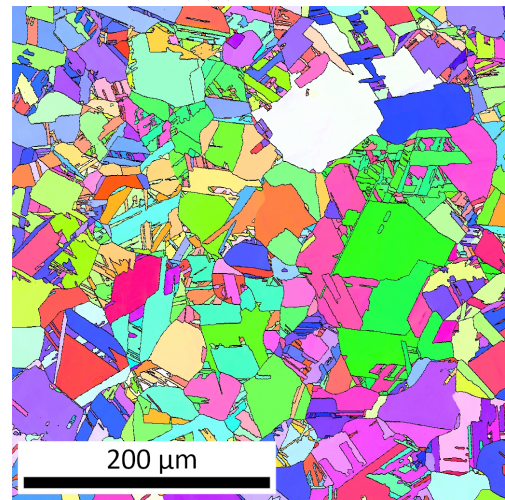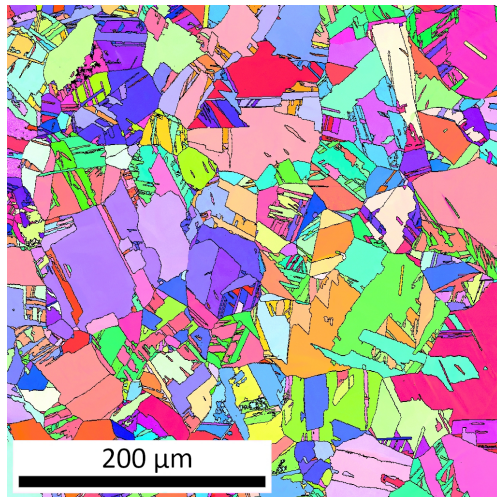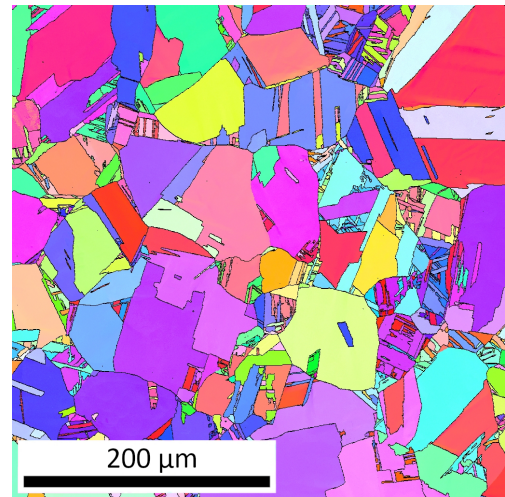
(d) co900

(e) co1000

(f) co1100

Figure 3.2: Orientation maps of samples after annealing acquired using EBSD.

(a) co600

(b) co700

(c) co800

(d) co900
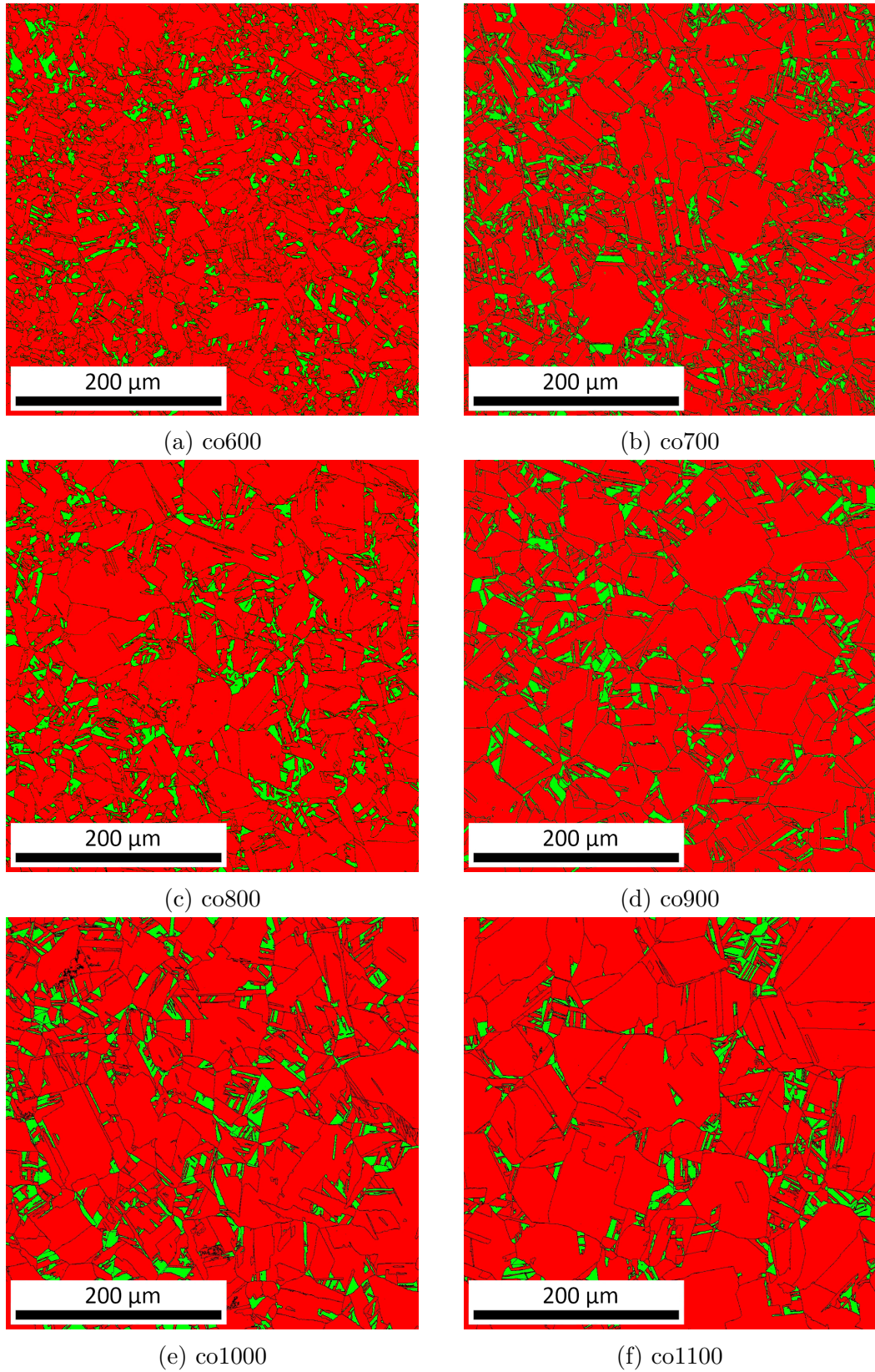
(e) co1000

(f) co1100

Figure 3.3: Phase maps of samples after annealing processed from EBSD.
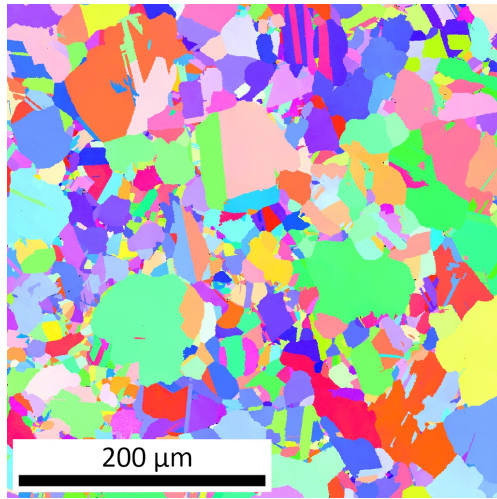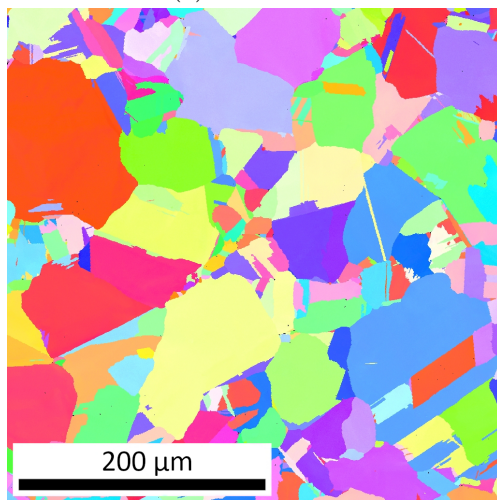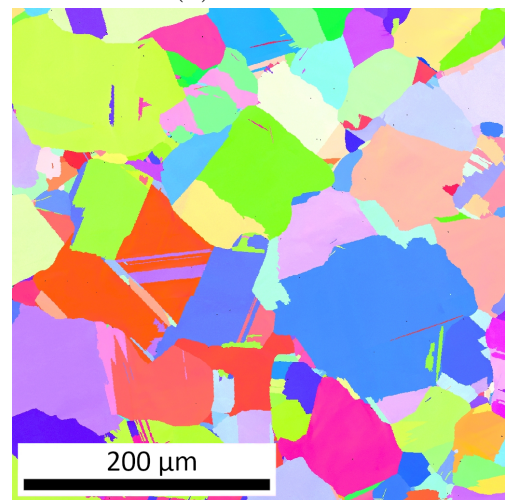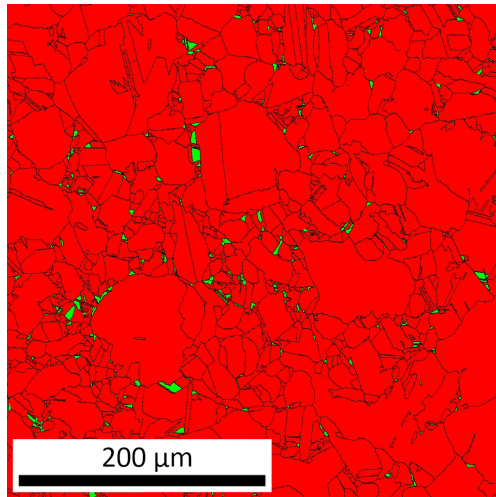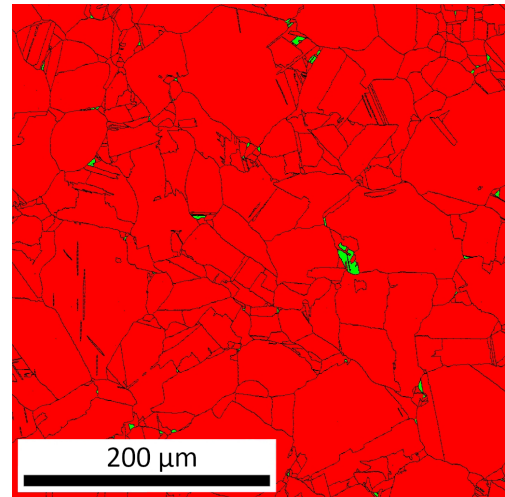
(a) co600-10c
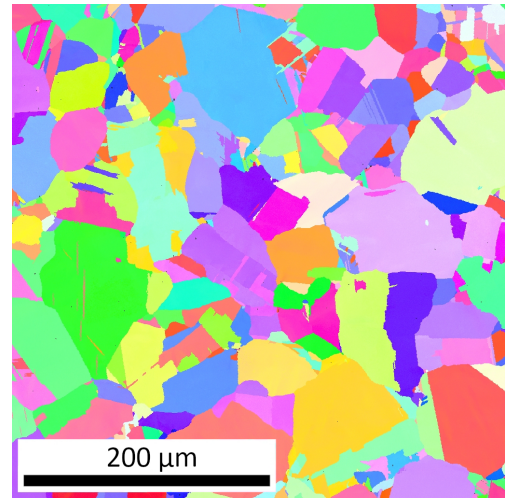
(b) co700-10c
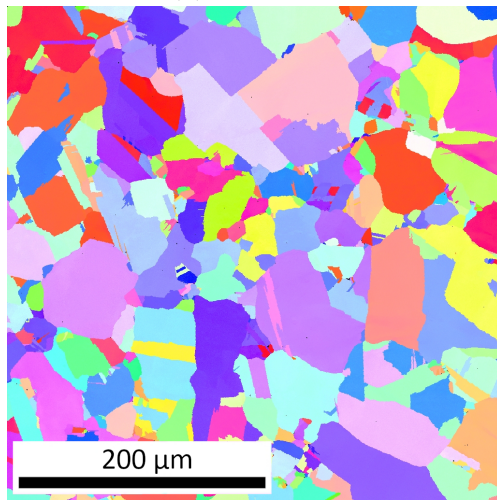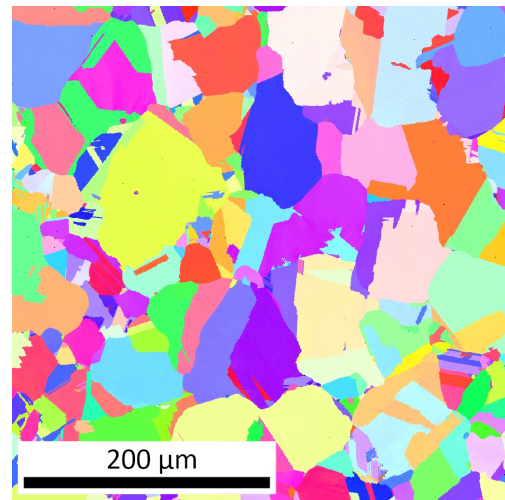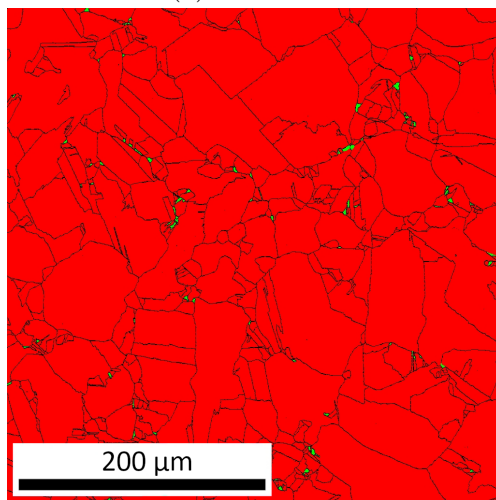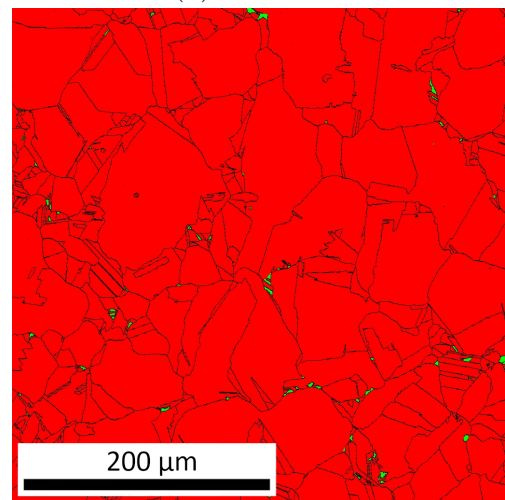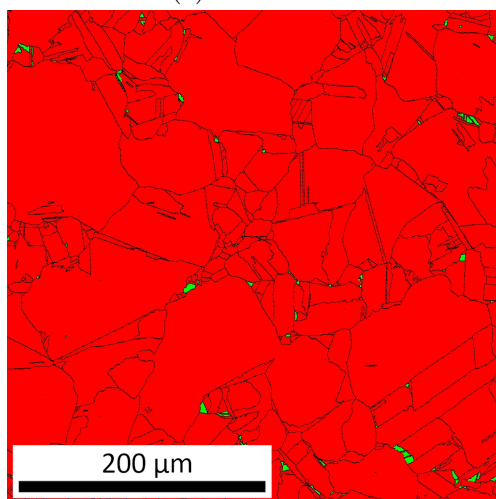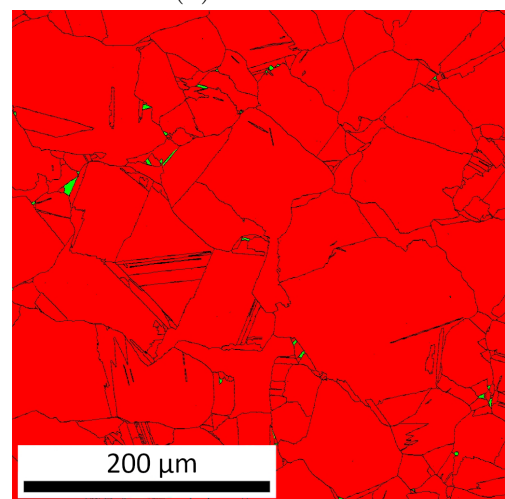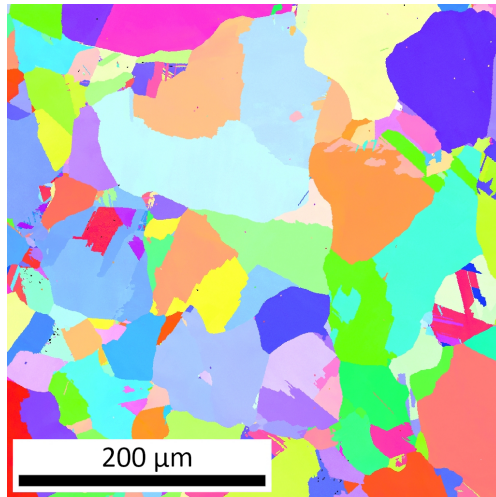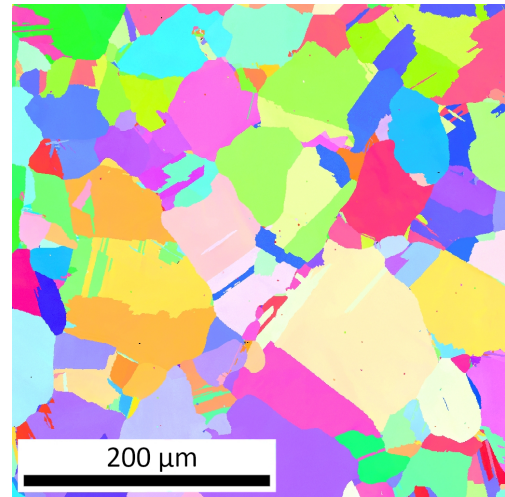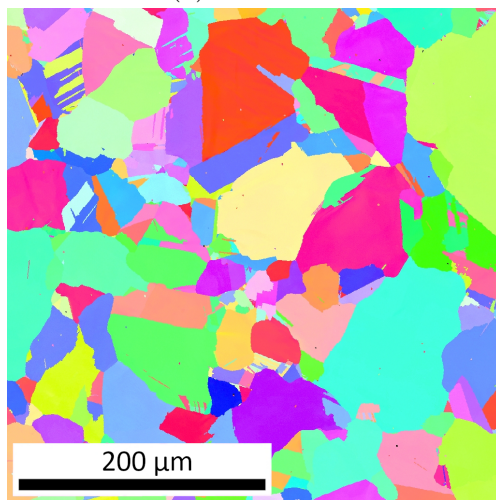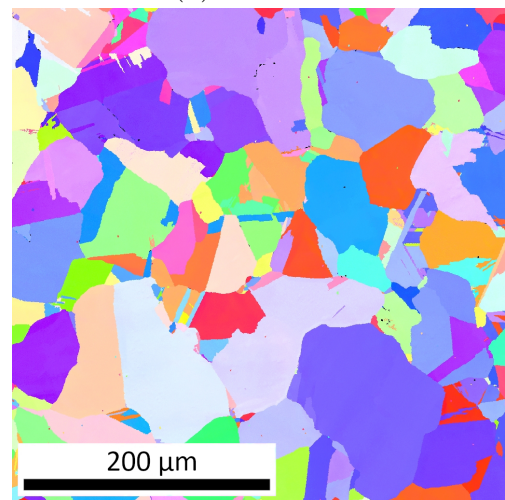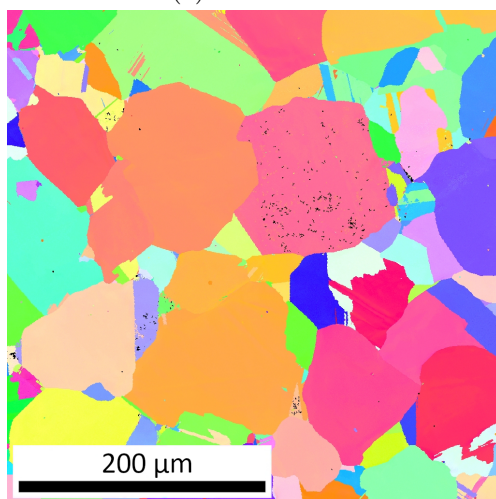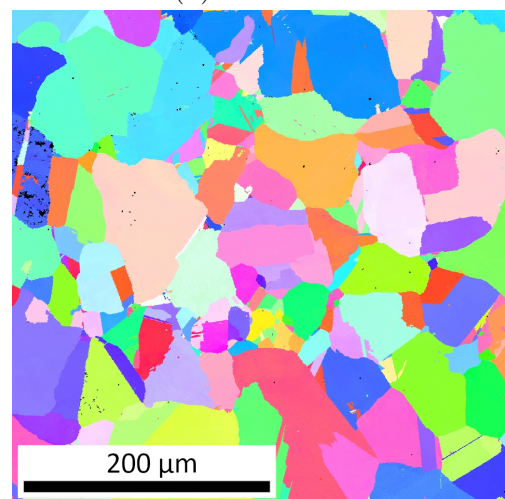
(c) co800-10c

(d) co900-10c

(e) co1000-10c

(f) co1100-10c

Figure 3.4: Orientation maps of samples after annealing and ten thermal cycles acquired using EBSD.

(a) co600-10c

(b) co700-10c

(c) co800-10c

(d) co900-10c

(e) co1000-10c

(f) co1100-10c

Figure 3.5: Phase maps of samples after annealing and ten thermal cycles processed from EBSD.
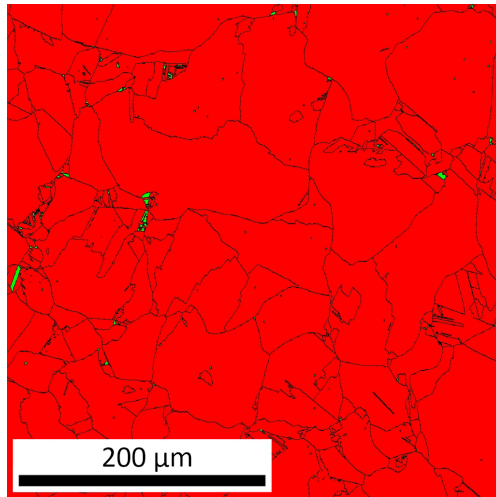
(a) co600-20c (b) co700-20c

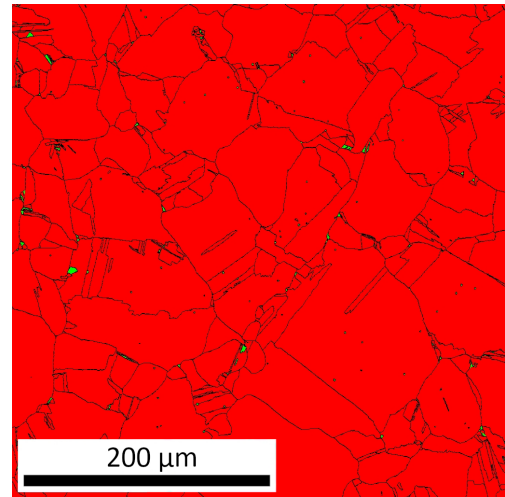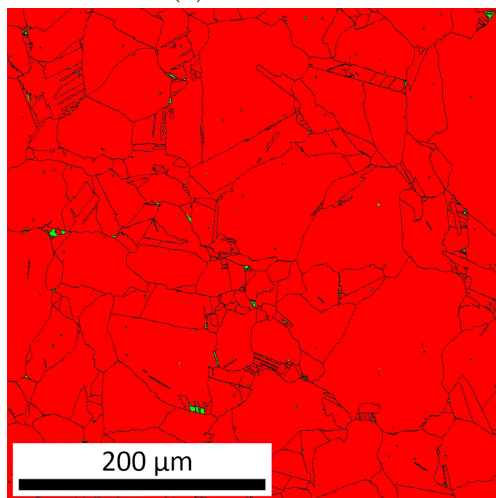(c) co800-20c (d) co900-20c

(e) co1000-20c (f) co1100-20c

Figure 3.6: Orientation maps of samples after annealing and twenty thermal cycles acquired using EBSD.
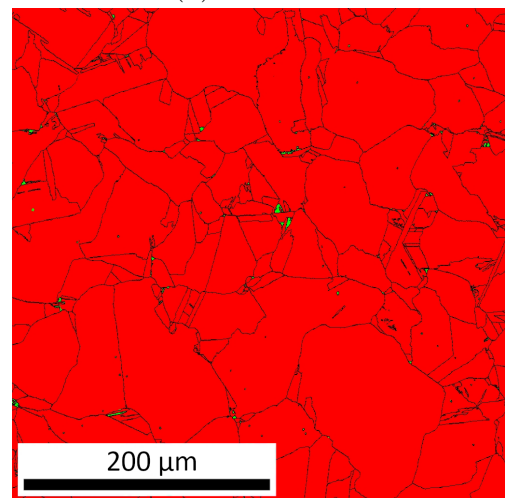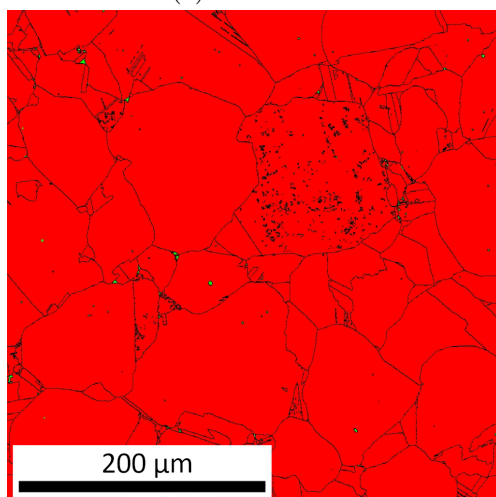
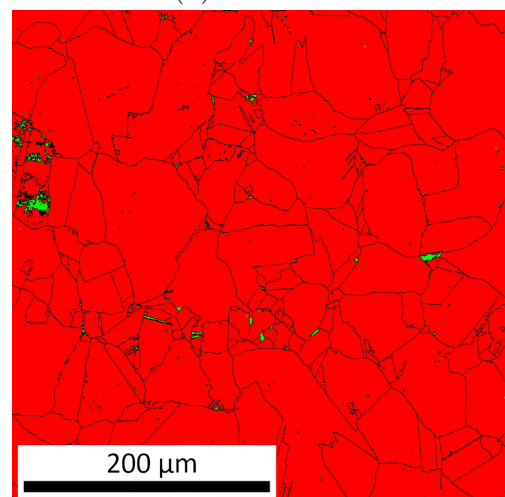(a) co600-20c   (b) co700-20c

(c) co800-20c   (d) co900-20c

(e) co1000-20c   (f) co1100-20c

Figure 3.7: Phase maps of samples after annealing and twenty thermal cycles processed from EBSD.

Table 3.1: Microstructural data of the samples as measured from the EBSD data.

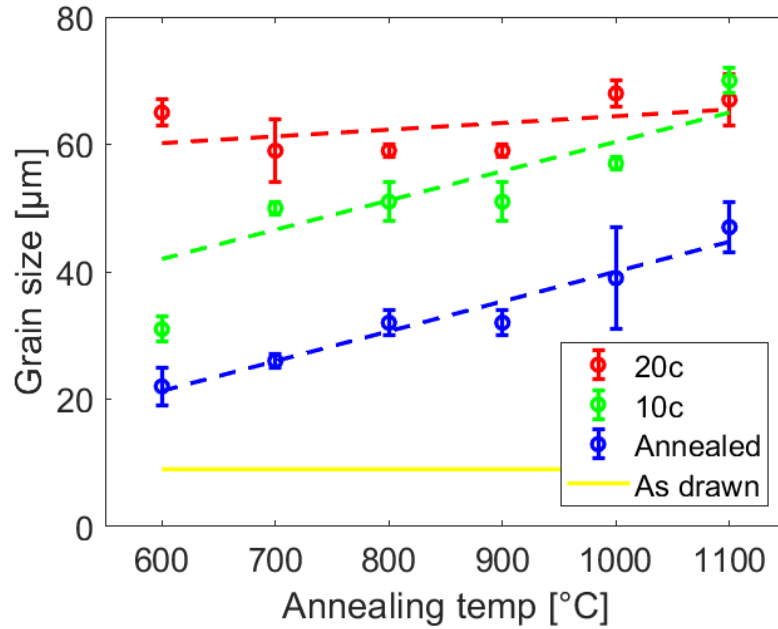| Sample	Grain size [µm]	fcc Fraction %
co600	22(3)	∼6
co700	26(1)	∼10
co800	32(2)	∼8
co900	32(2)	∼11
co1000	39(8)	∼11
co1100	47(4)	∼6
co600-10c	31(2)	∼1
co700-10c	50(1)	<0.5
co800-10c	51(3)	<0.5
co900-10c	51(3)	<0.5
co1000-10c	57(1)	<0.5
co1100-10c	70(2)	<0.5
co600-20c	65(2)	<0.5
co700-20c	59(5)	<0.5
co800-20c	59(1)	<0.5
co900-20c	59(1)	<0.5
co1000-20c	68(2)	<0.5
co1100-20c	67(4)	<0.5

Figure 3.8: Grain size dependence on thermal preparation. Annealing temperature of the initial annealing is on the x axis. Subsequent thermal cycling is indicated by the colour of the points.
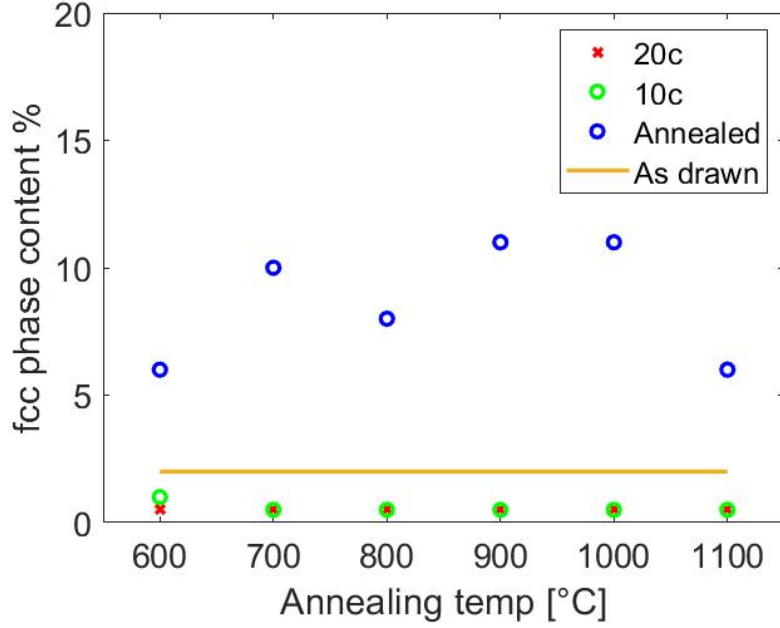
Figure 3.9: Effect of thermal preparation on residual fcc fraction. Annealing temperature of the initial annealing is on the x axis. Subsequent thermal cycling is indicated by the colour of the points.

3.2 Deformation tests

Figure 3.10 shows deformation curves of all annealed samples without thermal cycling. Table 3.2 contains the values of ε_{max}, σ_{max} and $\sigma_{0.2}$ for each type of tested sample. The $\sigma_{0.2}$ values of annealed samples decrease monotonously with higher annealing temperature from $\approx 422\,\mathrm{MPa}$ to $\approx 269\,\mathrm{MPa}$. Opposite trend is present in ε_{max} values, which increase with higher annealing temperature from $\approx 32\,\%$ to $\approx 38\,\%$. The value of σ_{max} varies slightly between $\approx 961\,\mathrm{MPa}$ and $\approx 1024\,\mathrm{MPa}$ and it does not show a clear dependence on annealing temperature. The σ_{max} of the co600 sample is an outlier at $\approx 1091\,\mathrm{MPa}$. Figure 3.11 shows deformation curves of all samples thermally cycled for ten cycles. Already there does not seem to be any clear dependence of mechanical properties on previous annealing temperature. The values of ε_{max} are between $\approx 27\,\%$ and $\approx 32\,\%$ and noticeably lower than in the not thermally cycled samples. A decrease is also observed in σ_{max} with values between $\approx 885\,\mathrm{MPa}$ and $\approx 926\,\mathrm{MPa}$. The values of $\sigma_{0.2}$ are all close to the $\sigma_{0.2}$ of co1100 with values ranging from $\approx 257\,\mathrm{MPa}$ to $\approx 287\,\mathrm{MPa}$. Even the sample co600-10c which was an outlier in observed microstructure does not seem to vary significantly. Figure 3.12 shows deformation curves of all samples thermally cycled for twenty cycles. The values of ε_{max} are again independent of previous annealing temperature and range from $\approx 25\,\%$ to $\approx 28\,\%$. Similarly the values of σ_{max} are also independent of previous annealing temperature and slightly lower than those for samples that were subject to ten cycles. These values range between $\approx 863\,\mathrm{MPa}$ and $\approx 885\,\mathrm{MPa}$. The values of $\sigma_{0.2}$ of samples that have undergone twenty thermal cycles are in a similar range to those of samples that have been thermally cycled ten times, this range being $\approx 254\,\mathrm{MPa}$ to $\approx 276\,\mathrm{MPa}$. It is observed that after twenty cycles the deformation curves of all samples are

even more similar. The change of the observed deformation curves after thermal cycling is illustrated on samples co1100, co1100-10c, co1100-20c in Figure 3.13.

Table 3.2: The values of ε_{max}, σ_{max}, $\sigma_{0,2}$ measured from deformation testing.

| Sample	ε_{max} %	σ_{max} [MPa]	$\sigma_{0,2}$ [MPa]
co600	32(1)	1091(33)	422(13)
co700	33(1)	961(29)	312(9)
co800	36(1)	984(30)	290(9)
co900	39(1)	1024(31)	283(8)
co1000	38(1)	1014(30)	274(8)
co1100	38(1)	1008(30)	269(8)
co600-10c	29(1)	918(28)	287(9)
co700-10c	32(1)	926(28)	277(8)
co800-10c	29(1)	895(27)	257(8)
co900-10c	27(1)	887(27)	261(8)
co1000-10c	31(1)	885(27)	267(8)
co1100-10c	32(1)	894(27)	276(8)
co600-20c	25(1)	879(26)	276(8)
co700-20c	28(1)	885(27)	268(8)
co800-20c	26(1)	878(26)	268(8)
co900-20c	28(1)	879(26)	259(8)
co1000-20c	26(1)	863(26)	267(8)
co1100-20c	27(1)	864(26)	254(8)
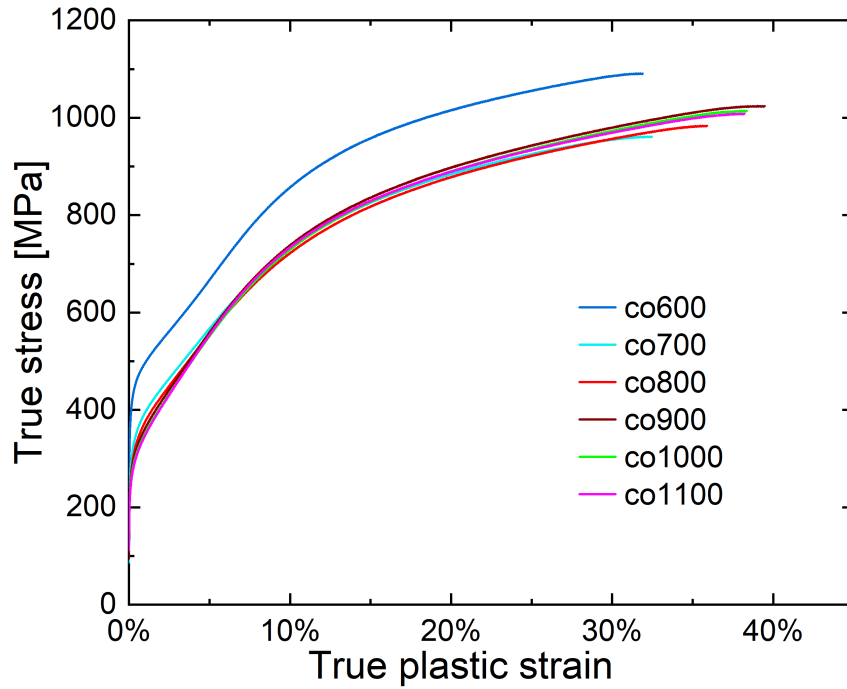
Figure 3.10: The deformation curves of all samples that have been annealed without thermal cycling.
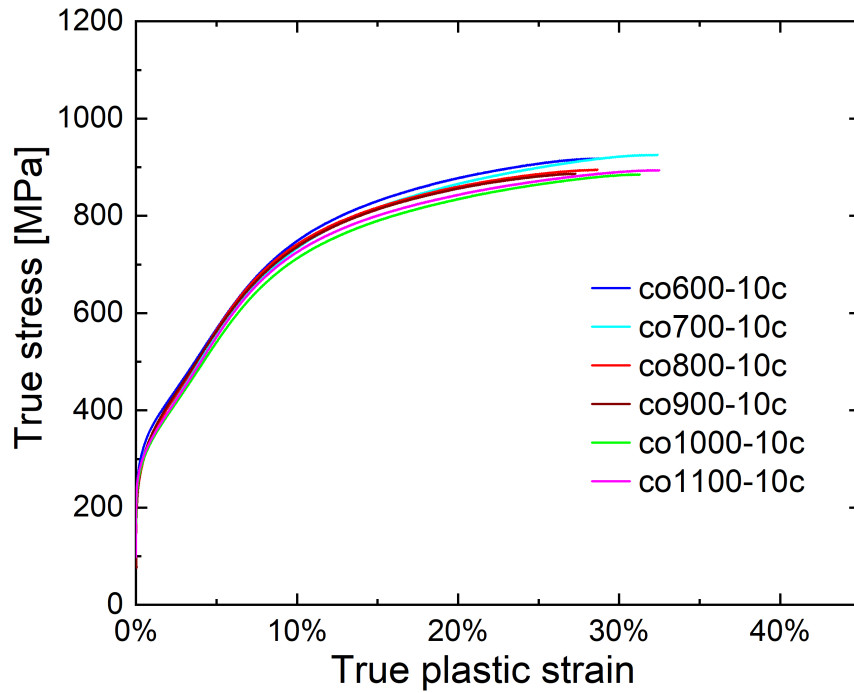
Figure 3.11: The deformation curves of all samples that have been annealed and subjected to ten thermal cycles.
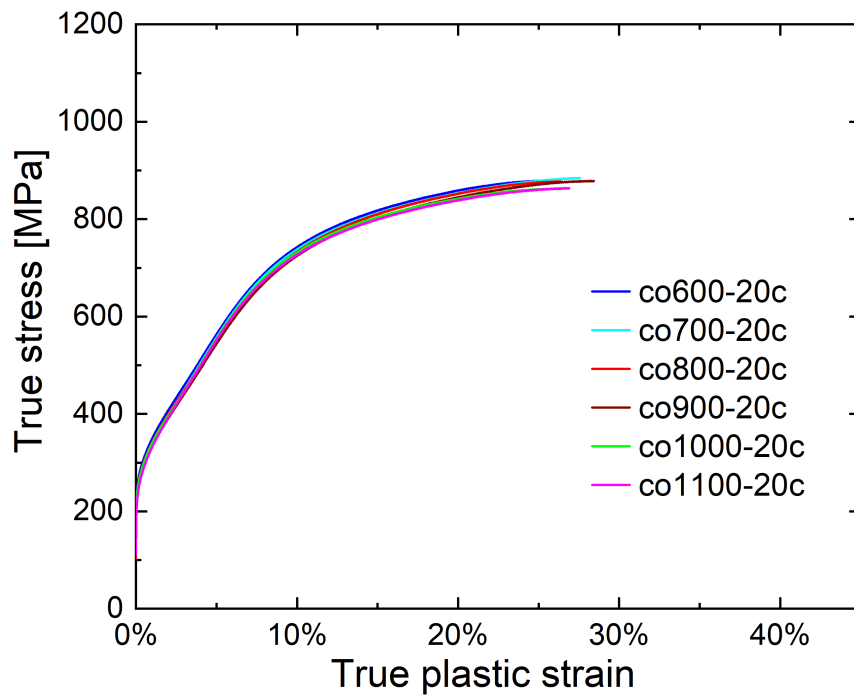

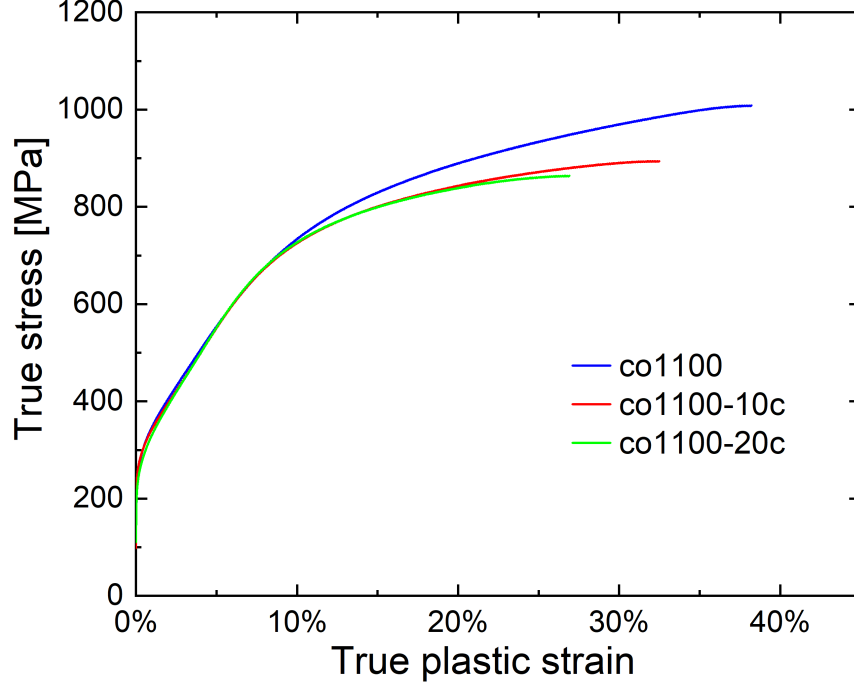Figure 3.12: The deformation curves of all samples that have been annealed and subjected to twenty thermal cycles.

Figure 3.13: Chosen deformation curves illustrating the effect of thermal cycling on mechanical properties.

3.3 Acoustic emission

Figure 3.14 shows the evolution of maximum amplitude of AE events during deformation of annealed samples on a logarithmic scale. The graphs also show a curve of engineering strain for comparison. Nearly all activity (aside from cracking induced AE observed at the end of the experiment) is concentrated in the early stages of deformation. The amplitudes are already high during the elastic phase of the deformation and events continue to be detected beyond yield point. After this active interval only a few sporadic events appear until cracking and the end of the test. Maximum amplitude observed increases with higher annealing temperature. As can be seen in Figures 3.15 3.16, samples that were also subjected to thermal cycling show both slightly higher amplitudes and longer window of activity compared to the co1100 sample. As is the case with deformation curves, there is no significant dependence on previous annealing temperature observed for these thermally cycled samples. Unlike deformation curves there is not a significant dependence on the number of cycles. Figure 3.17 shows the CCDF distribution of amplitude of events squared A^2 fitted with a power law for annealed samples. All of these distributions exhibit the fitted coefficient α_{ML} from ≈ 1.87 to ≈ 1.95. The tail end of the distributions falls off the fitted curve. This is a common feature of power law distributions, as by the definition of CCDF the distribution ends at zero. At the same time the probability of large events is limited by the finite size of the sample and grains in the sample. Figures 3.18 and 3.19 show the distribution of A^2 for samples that were subject to ten and twenty cycles of thermal cycling respectively. The fitted coefficients α_{ML} are lower after thermal cycling. After ten cycles the coefficients α_{ML} range from ≈ 1.70 to

≈ 1.87. In the case of samples subjected to twenty cycles the range is from ≈ 1.77 to ≈ 1.86, which is within the range of α_{ML} of samples cycled for ten cycles. All of the α_{ML} values are summarised in Table 3.3.
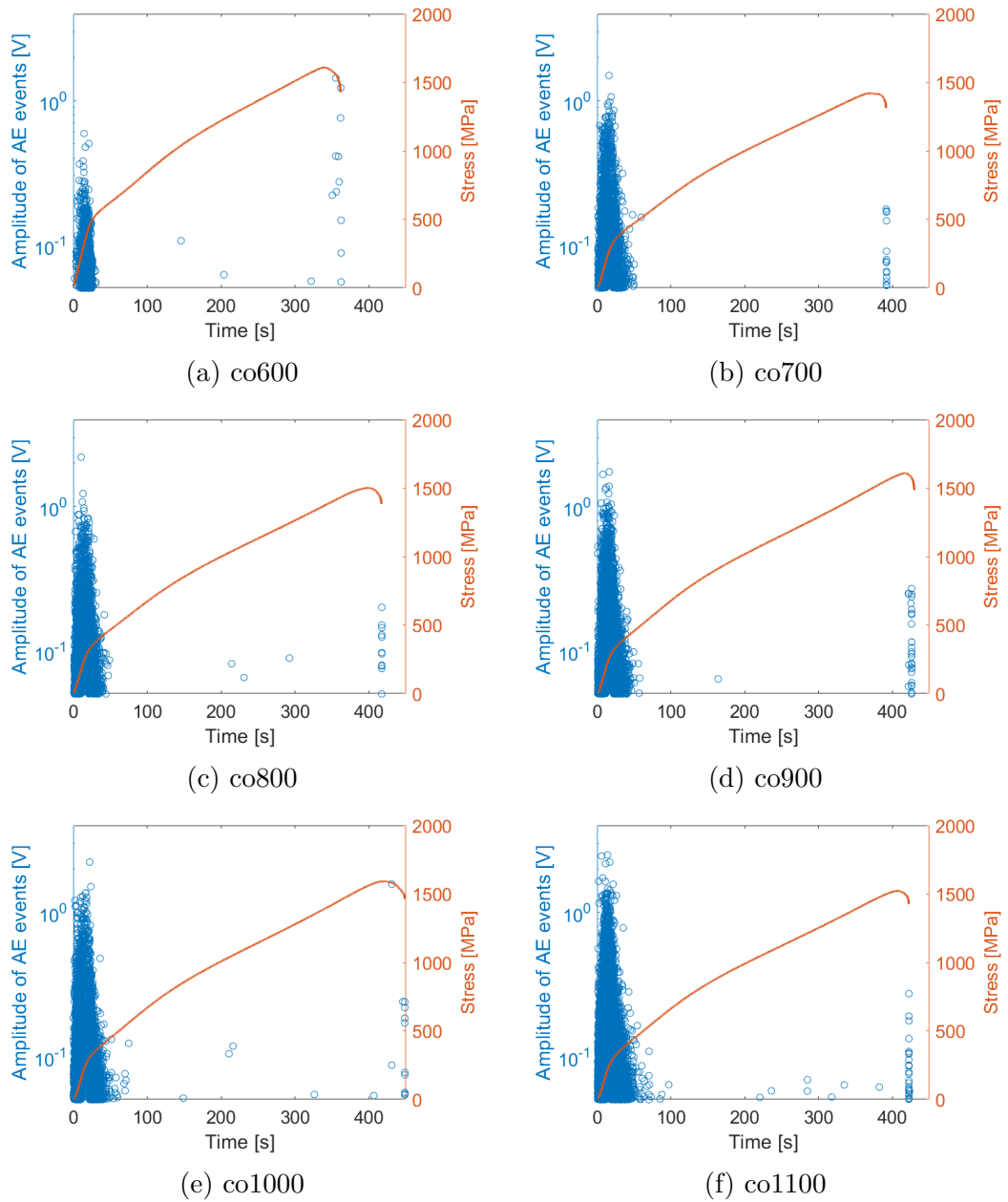

Figure 3.14: Amplitude of AE events on a logarithmic scale in relation to time with deformation curve added for comparison for each type of annealed sample.
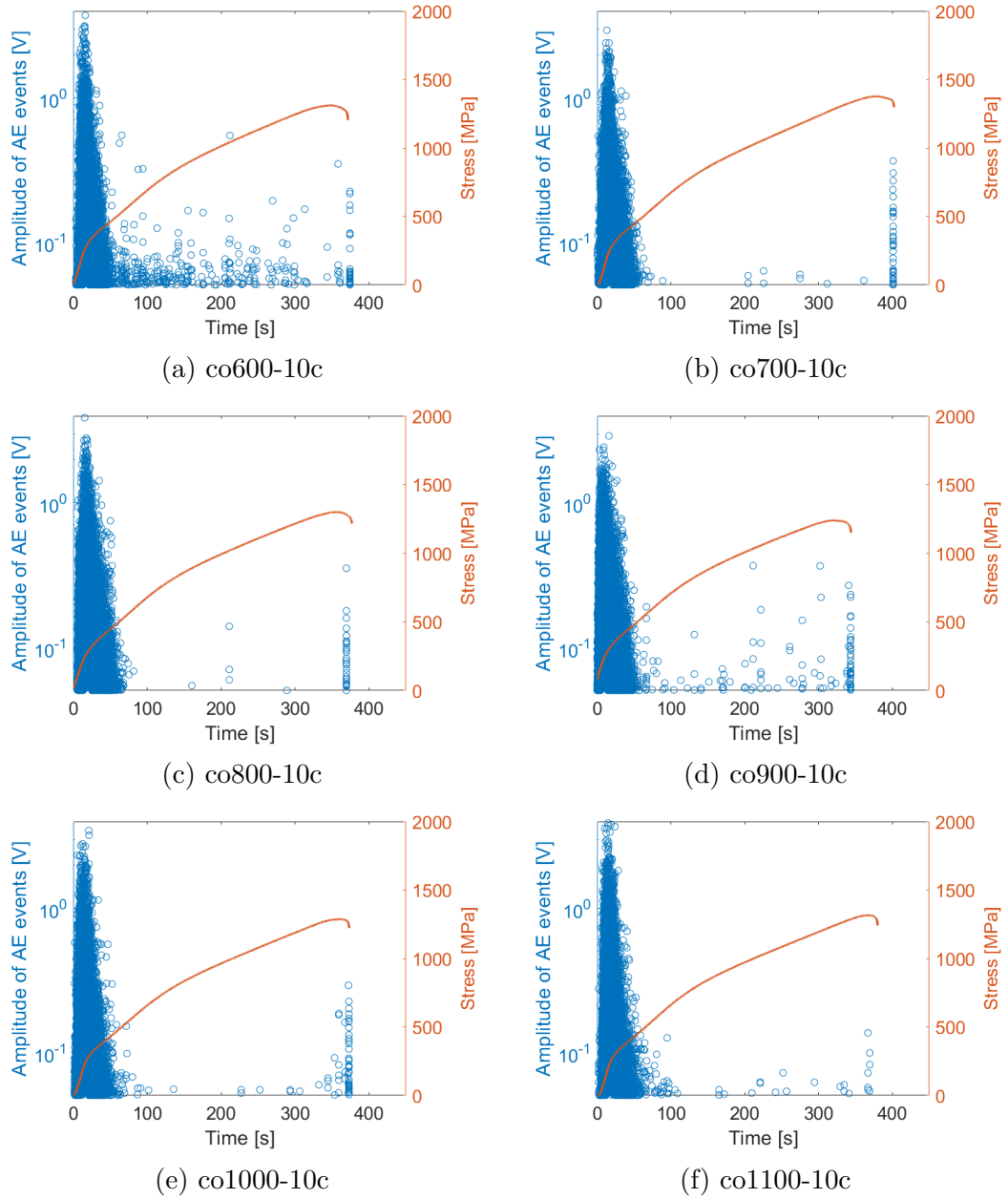
Figure 3.15: Amplitude of AE events on a logarithmic scale in relation to time with deformation curve added for comparison for samples that have been annealed and thermally cycled for ten cycles.
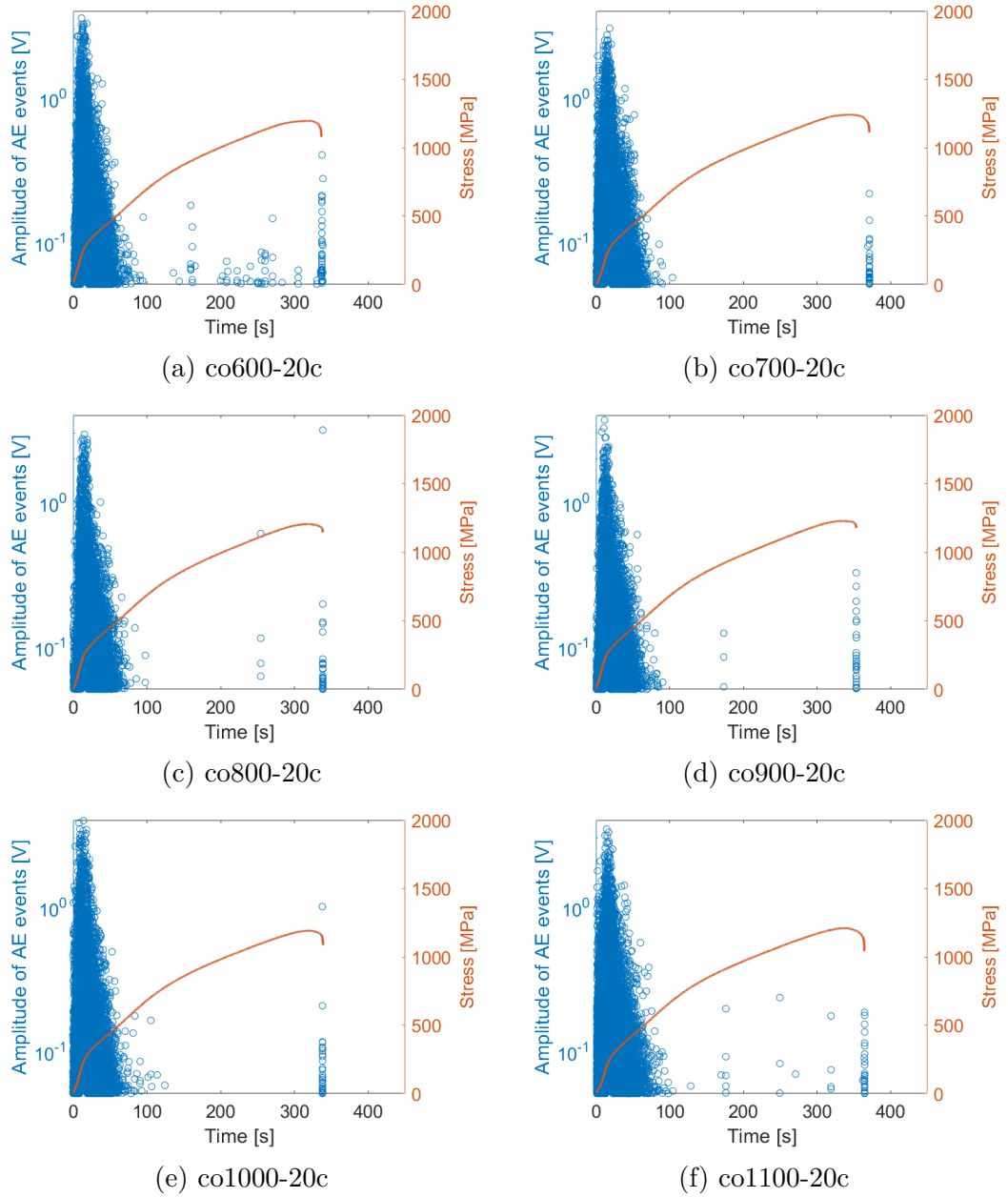
(a) co600-20c

(b) co700-20c

(c) co800-20c

(d) co900-20c

(e) co1000-20c

(f) co1100-20c

Figure 3.16: Amplitude of AE events on a logarithmic scale in relation to time with deformation curve added for comparison for samples that have been annealed and thermally cycled for twenty cycles.
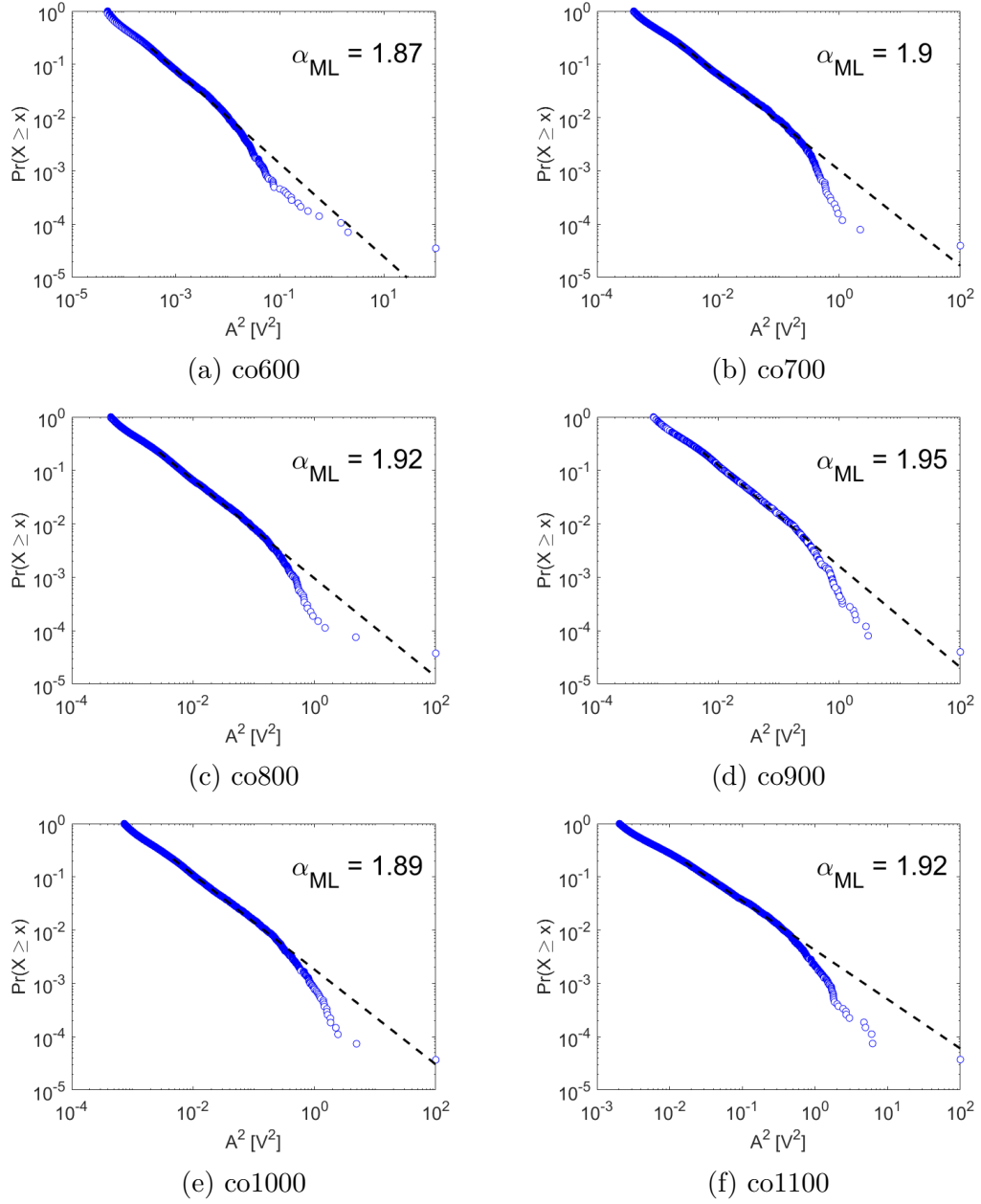
Figure 3.17: Power law fitted distributions observed in the values of amplitude squared of AE events for each type of annealed sample.
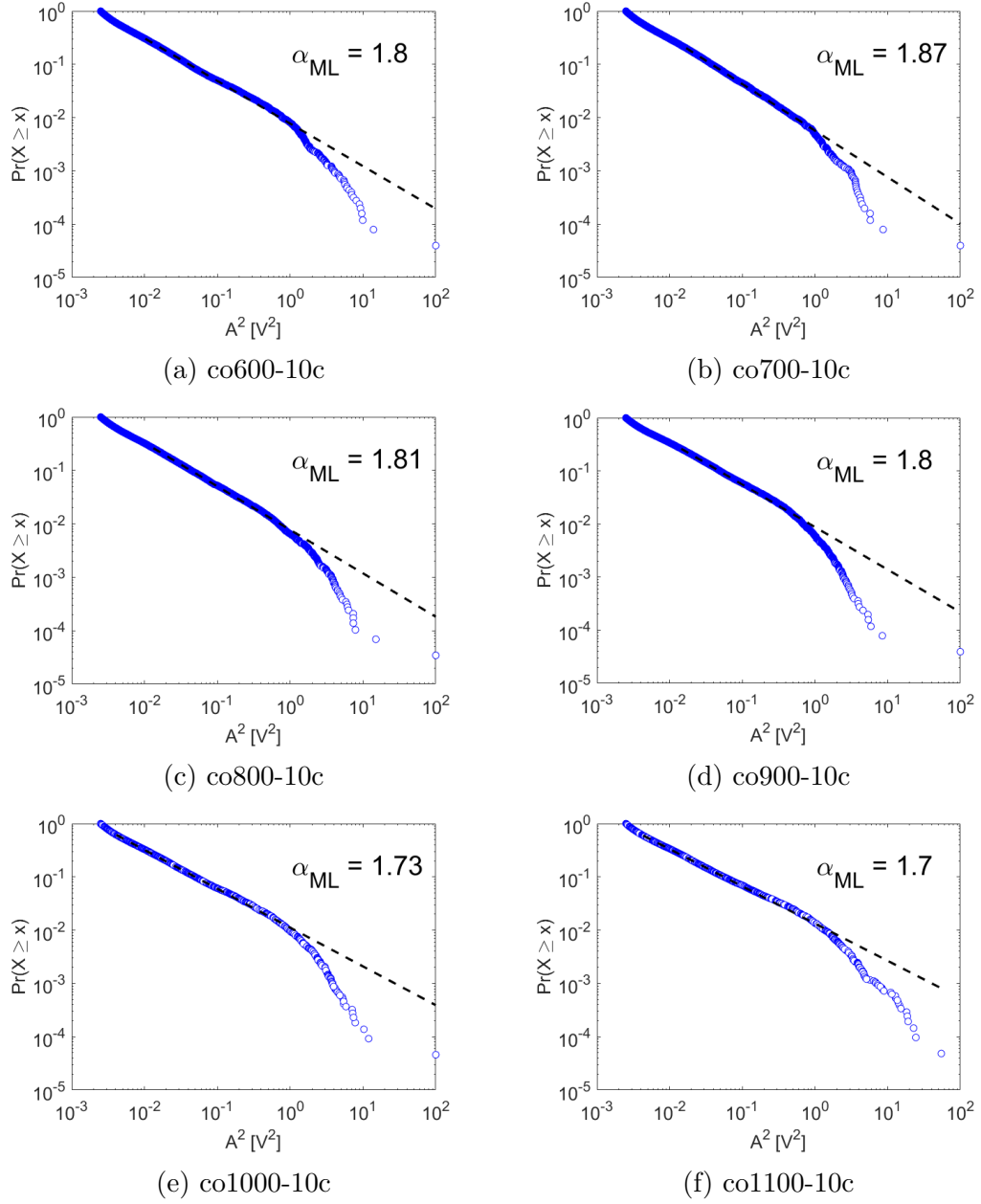
Figure 3.18: Power law fitted distributions observed in the values of amplitude squared of AE events for samples that have been annealed and thermally cycled for ten cycles.
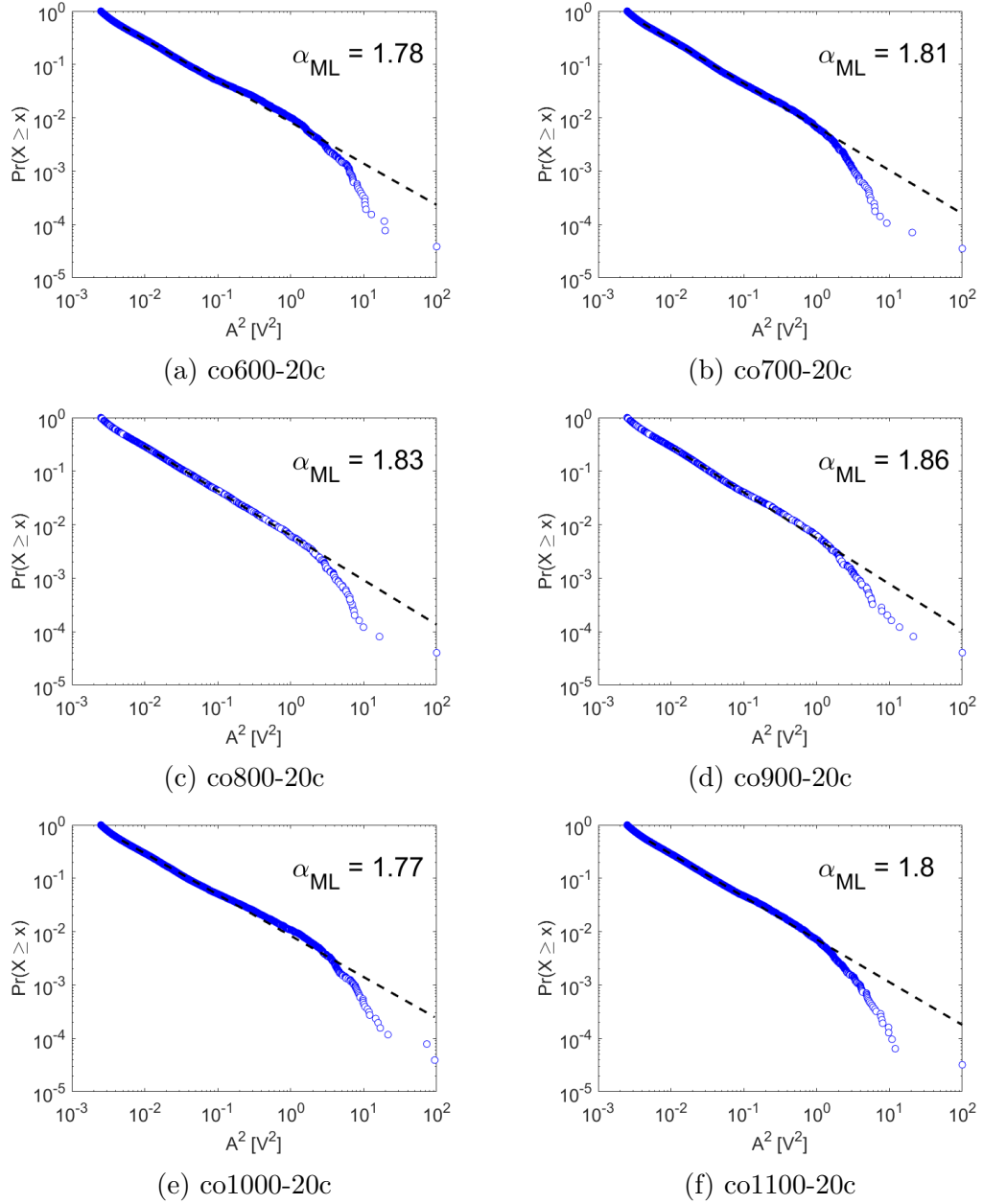
Figure 3.19: Power law fitted distributions observed in the values of amplitude squared of AE events for samples that have been annealed and thermally cycled for twenty cycles.

Table 3.3: The α_{ML} coefficients obtained through fitting of the A^2 distributions.

Sample	α_{ML}	Sample	α_{ML}	Sample	α_{ML}
co600	1.87	co600-10c	1.80	co600-20c	1.78
co700	1.90	co700-10c	1.87	co700-20c	1.81
co800	1.92	co800-10c	1.81	co800-20c	1.83
co900	1.95	co900-10c	1.80	co900-20c	1.86
co1000	1.89	co1000-10c	1.73	co1000-20c	1.77
co1100	1.92	co1100-10c	1.70	co1100-20c	1.80

3.4 Interrupted deformation

Four selected types of samples were also investigated using a deformation test interrupted at several points to acquire EBSD data. During these interrupted deformation tests, EBSD data was acquired on the initial state before deformation and then at 1 %, 4 %, 10 %, 20 % and 30 % engineering strain. These values of strain are shown intersecting the deformation curves of the samples in Figure 3.20. The samples selected were co600, co800, co1100 with the aim to observe the impact of annealing temperature and the co1100-20c sample to observe the impact of thermal cycling. The EBSD data was further utilised to determine the evolution of fcc phase content, KAM and twin volume fraction during deformation in order to shed more light on the effects observed in the deformation and AE results. Table 3.4 contains a summary of these values. While EBSD was also measured at 20 % and 30 % engineering strain, these results are less accurate because of high number of low CI points present on those EBSD maps. In the case of co600 the fine grain microstrucutre combined with deformation render the 20 % and 30 % engineering strain measurements unusable. The figures 3.22, 3.24, 3.26 and 3.28 show the orientation maps of the samples investigated using the interrupted deformation method and how they evolve during deformation. All samples tested this way show activation of $\{10\bar{1}2\}$ type twinning. These twins initially appear lenticular shaped and subsequently some of them grow during further deformation, in some cases completely or almost completely replacing the parent grain. The $\{11\bar{2}1\}$ type twinning is also present in a few grains in the deformed states of the co800 sample. These twins appear in a "zig-zag" pattern inside the parent grain, as can be seen in Figures 3.24 and 4.2. These twins only appear from 4 % strain onward consistent with their higher CRSS, and also do not visibly grow during the remainder of the deformation.

The evolution of fcc fraction, twin volume fraction and KAM is further quantified. The evolution of fcc fraction in Figure 3.30 shows a clear decrease during deformation. The rate at which the fcc phase fraction decreases is higher in the case of higher initial values. During deformation the transformation slows down and the samples still contain a part of the initially present fcc phase when the test ends. It is important to note however that the fcc fraction is determined using only points with CI > 0.1. Since CI deteriorates in heavily deformed areas this could introduce a systematic error if the fcc regions were disproportionately affected by the decrease in CI. Judging by the phase maps acquired this does not seem to be the case, but it cannot be completely ruled out. Low CI points however only start to appear more frequently in the data after 10 % of deformation. The evolution of KAM presented in Figure 3.31 shows a rise in KAM during deformation. The exception is the first point at 1 % engineering strain, which shows little or no change in KAM. As KAM is closely related to dislocation density this would as expected confirm minimal activation of slip before yield point. Upon further deformation there is a clear increase, which slows down in the later stages as the dislocation density and barriers to dislocation motion make further slip more difficult. Figure 3.32 shows the evolution of twin volume fraction during deformation. The first two points of measurement show very little or no twins present. Most twin nucleation happens between the 1 % strain point and 10 % point, with few or no new twins appearing after 10 %. The increase

in twin volume fraction between 4 % point and 10 % point is a mix of twin nucleation and twin growth and further increase can be attributed predominantly to twin growth. Interpreting the twin data requires extra caution as the detection of twins is not fully reliable especially in smaller grains that offer few pixels that could be used to determine the presence of the specific geometric relation present in twin-parent grain pairs. With continuing twin growth, occasionally twins mostly or completely replace the parent grain. Also further deformation may lead to degradation of image quality and the precision with which the geometric relations are detected. Because of this manual corrections are necessary for the more deformed states where the automatic detection starts to fail. This may introduce some systematic error into the observed values.
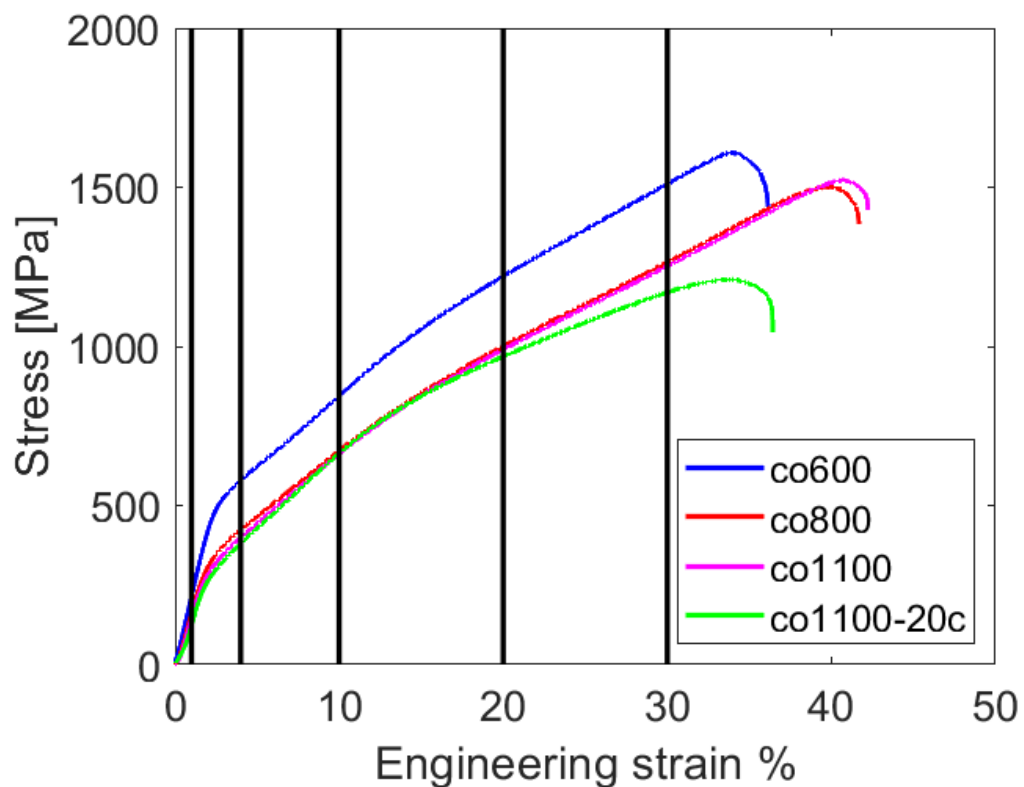

Figure 3.20: Coloured lines show deformation curves of the four samples chosen for interrupted deformation experiment. The vertical black lines are the values of engineering strain at which the deformation test was interrupted and EBSD data were acquired.

Table 3.4: Twin volume fraction, fcc fraction, KAM values resulting from EBSD acquired during interrupted deformation. Note that the decreasing precision of twin fraction determination with higher degree of deformation stems from the declining CI values.

| Sample	Strain %	Twin fraction %	fcc Fraction %	KAM °
co600	0	0.44(1)	~17.6	0.41(2)
co600	1	0.63(2)	~17.3	0.45(2)
co600	4	13.5(8)	~15.0	0.71(4)
co600	10	21(2)	~11.7	1.22(7)
co800	0	0.00	~14.2	0.39(2)
co800	1	0.04	~13.6	0.35(2)
co800	4	7.2(4)	~12.8	0.55(4)
co800	10	19(2)	~10.6	0.84(6)
co800	20	20(2)	~8.2	1.01(6)
co800	30	20(2)	~6.8	1.07(6)
co1100	0	0.00	~6.2	0.36(1)
co1100	1	0.04	~6.1	0.36(2)
co1100	4	10.0(6)	~5.5	0.58(4)
co1100	10	18(2)	~4.5	0.83(6)
co1100	20	21(2)	~3.5	1.01(6)
co1100	30	23(2)	~3.2	1.09(6)
co1100-20c	0	0.00	~0.3	0.38(2)
co1100-20c	1	0.07	~0.3	0.34(1)
co1100-20c	4	8.6(5)	~0.3	0.50(4)
co1100-20c	10	19(2)	~0.2	0.71(5)
co1100-20c	20	24(2)	~0.3	0.91(6)
co1100-20c	30	26(2)	~0.2	0.99(6)
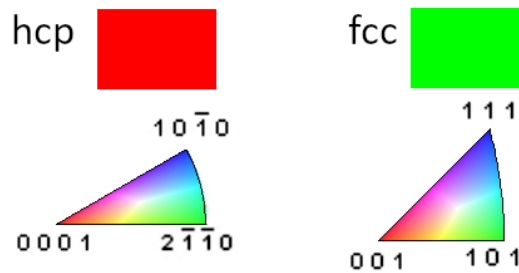
Figure 3.21: A key for the following orientation and phase maps. The map plane of all the EBSD maps in this section is parallel with both the drawing direction of the rod and loading direction. Compressive load was applied in a direction vertical on the page.
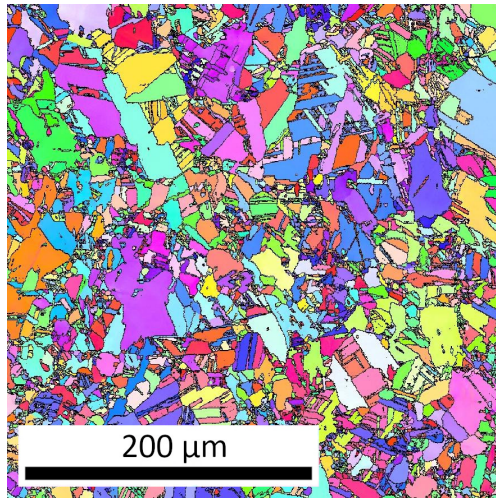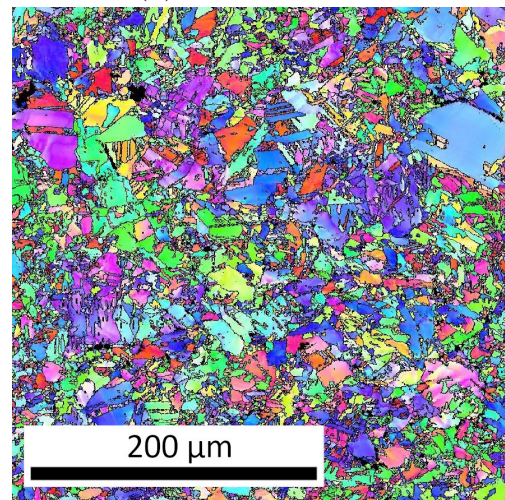
(a) Before deformation
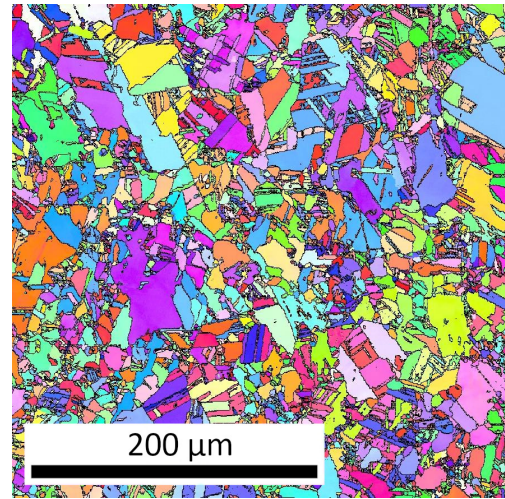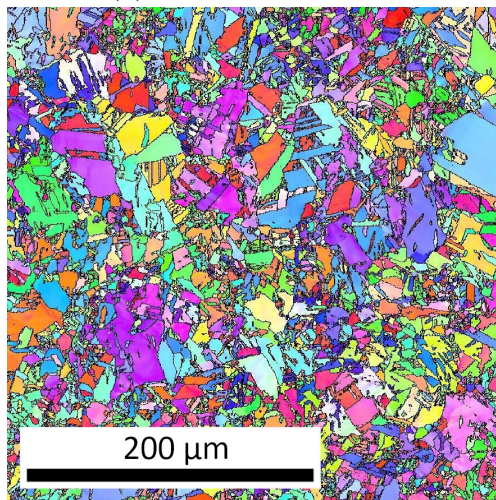
(b) 1 % eng. strain

(c) 4 % eng. strain

(d) 10 % eng. strain

Figure 3.22: Orientation maps acquired using EBSD during interrupted deformation experiment on the sample co600.

(a) Before deformation

(b) 1 % eng. strain
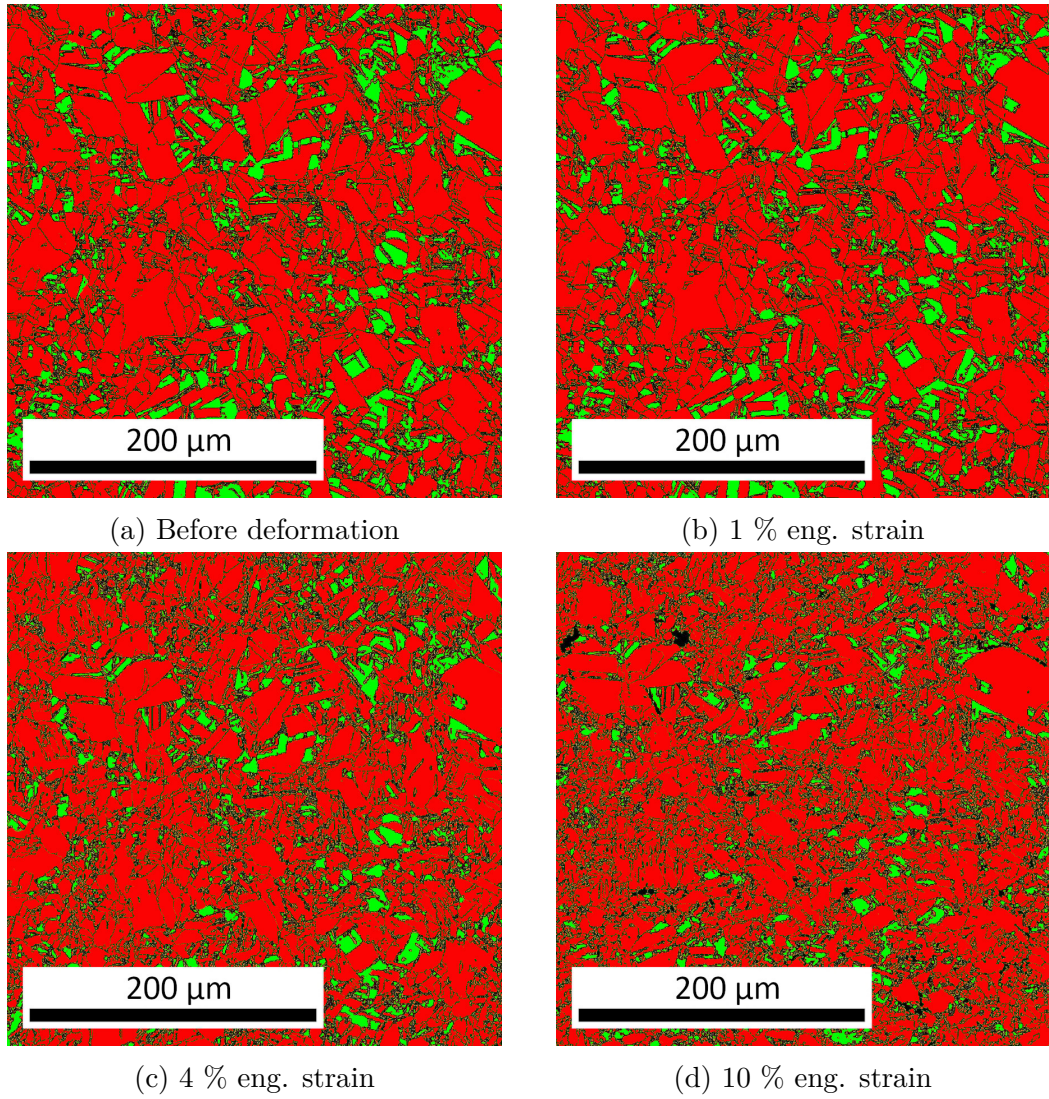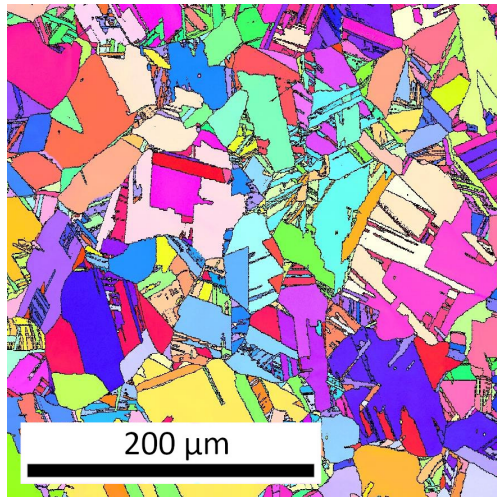
(c) 4 % eng. strain
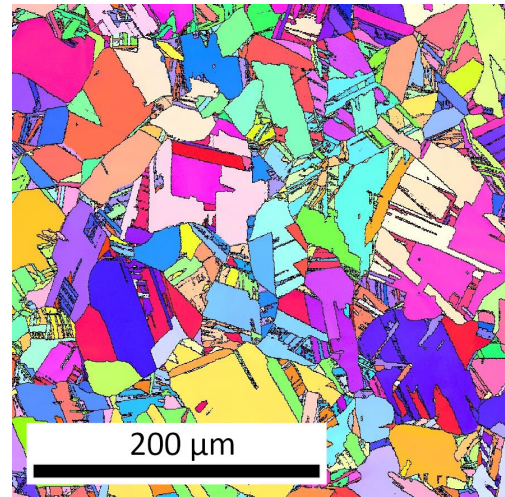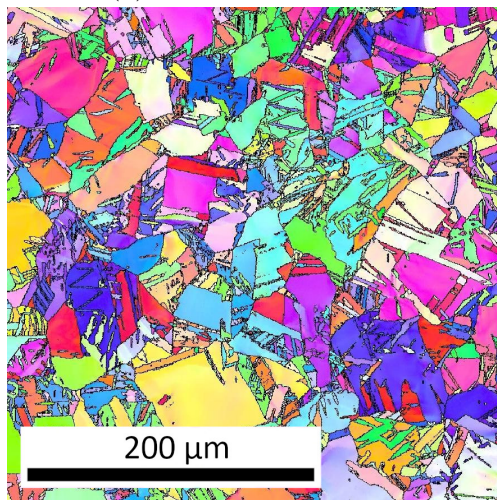
(d) 10 % eng. strain

Figure 3.23: Phase maps extracted from EBSD acquired during interrupted deformation experiment on the sample co600.
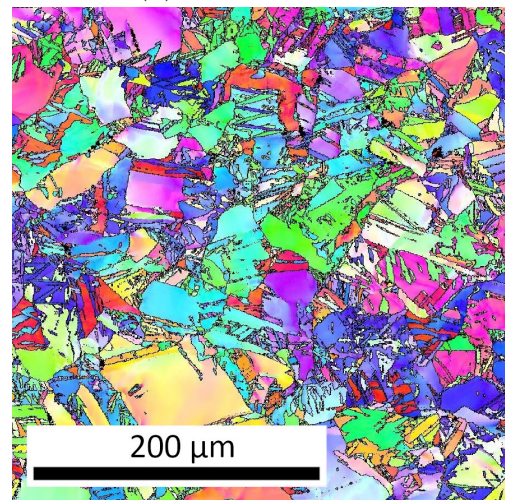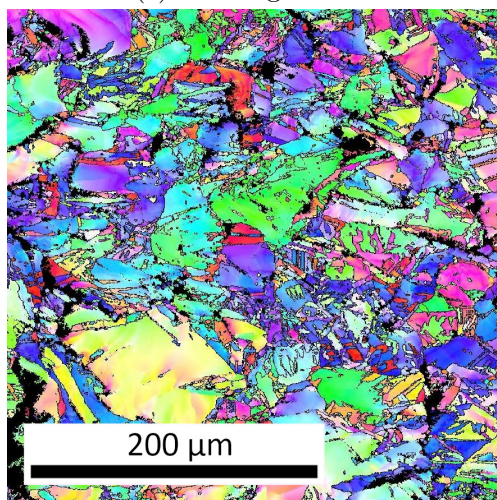
(a) Before deformation

(b) 1 % eng. strain

(c) 4 % eng. strain

(d) 10 % eng. strain

(e) 20 % eng. strain

(f) 30 % eng. strain

Figure 3.24: Orientation maps acquired using EBSD during interrupted deformation experiment on the sample co800.

(a) Before deformation

(b) 1 % eng. strain

(c) 4 % eng. strain

(d) 10 % eng. strain

(e) 20 % eng. strain

(f) 30 % eng. strain

Figure 3.25: Phase maps extracted from EBSD acquired during interrupted deformation experiment on the sample co800.

(a) Before deformation
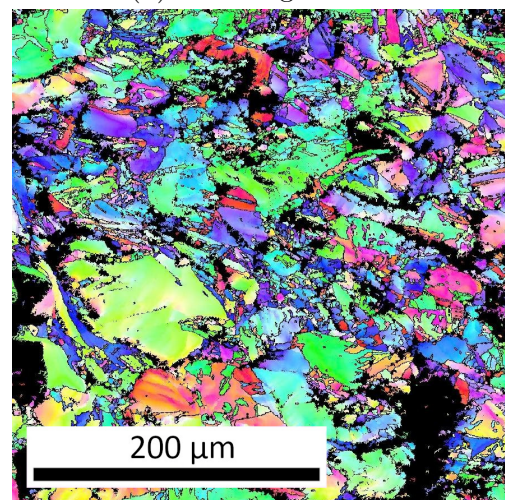
(b) 1 % eng. strain

(c) 4 % eng. strain

(d) 10 % eng. strain
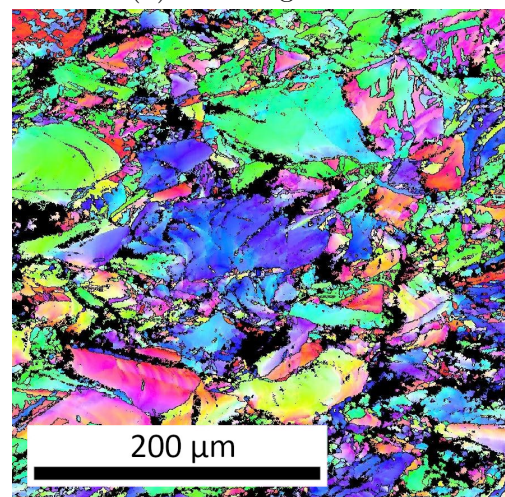
(e) 20 % eng. strain

(f) 30 % eng. strain

Figure 3.26: Orientation maps acquired using EBSD during interrupted deformation experiment on the sample co1100.

(a) Before deformation

(b) 1 % eng. strain

(c) 4 % eng. strain

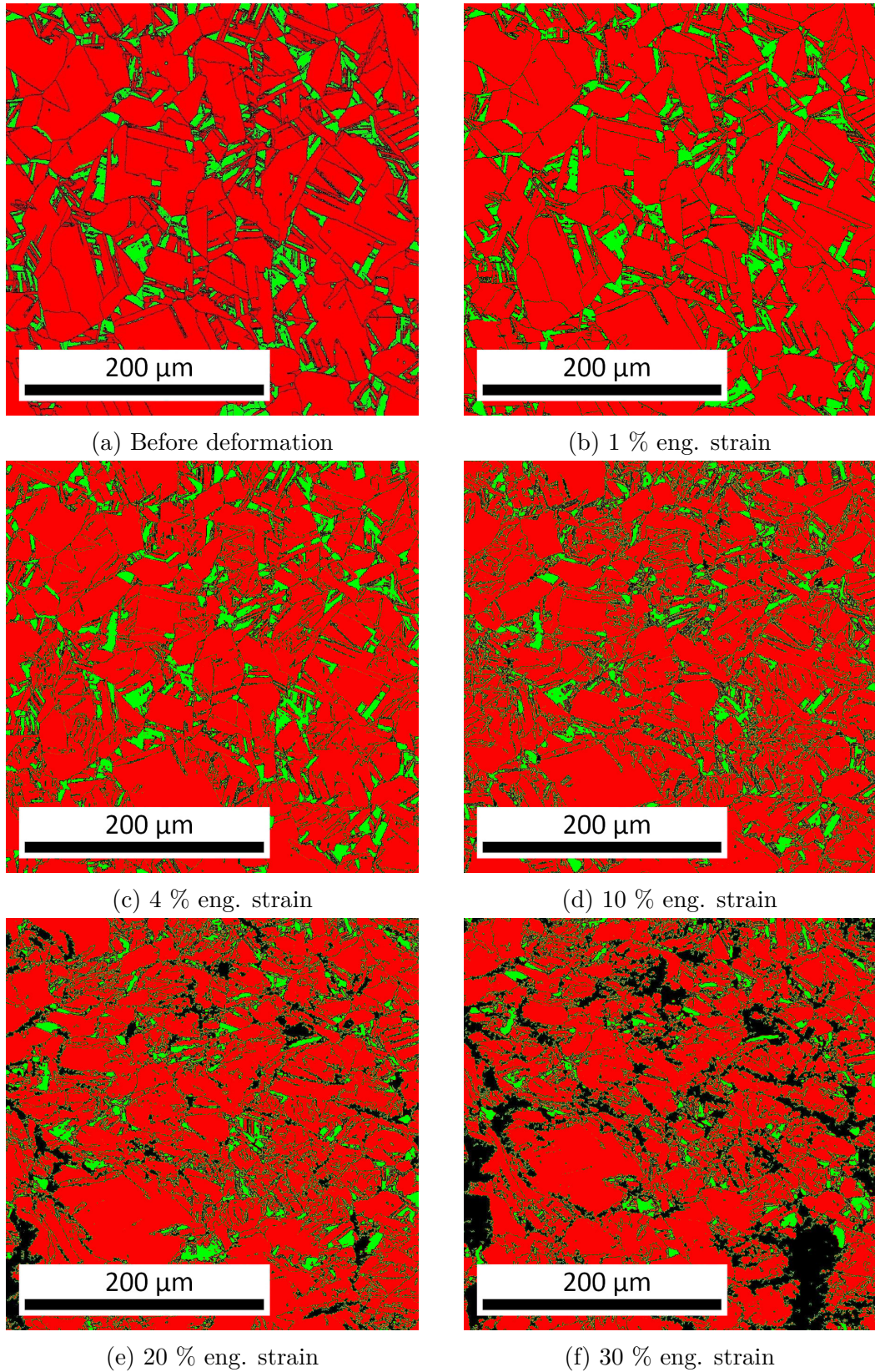(d) 10 % eng. strain

(e) 20 % eng. strain
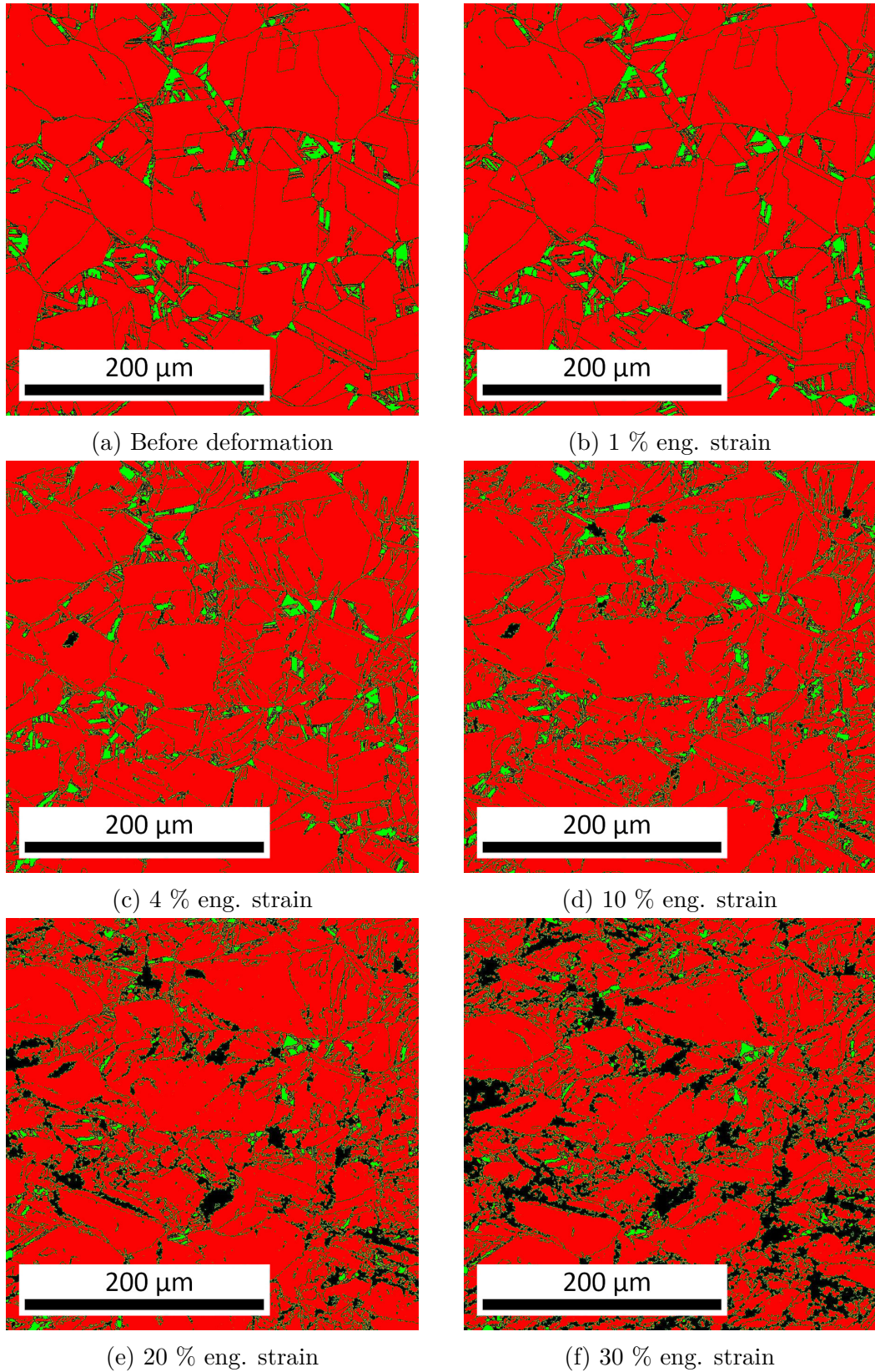
(f) 30 % eng. strain

Figure 3.27: Phase maps extracted from EBSD acquired during interrupted deformation experiment on the sample co1100.
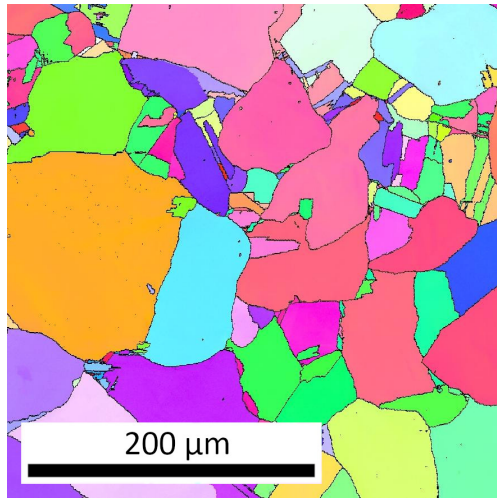
(a) Before deformation
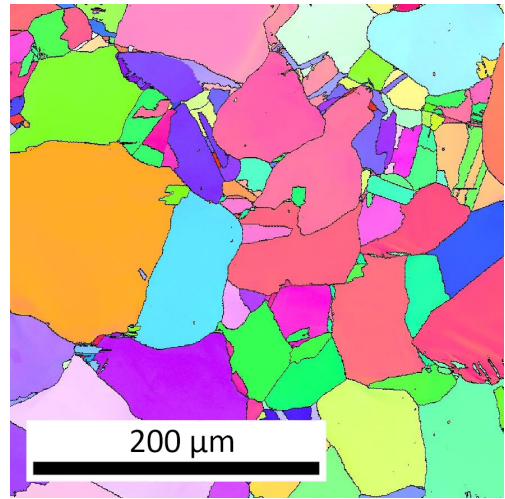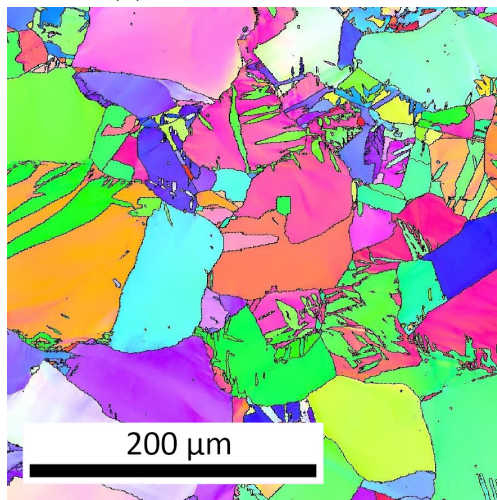
(b) 1 % eng. strain
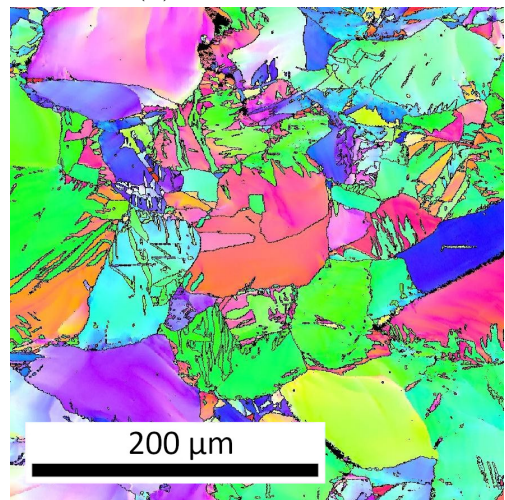
(c) 4 % eng. strain
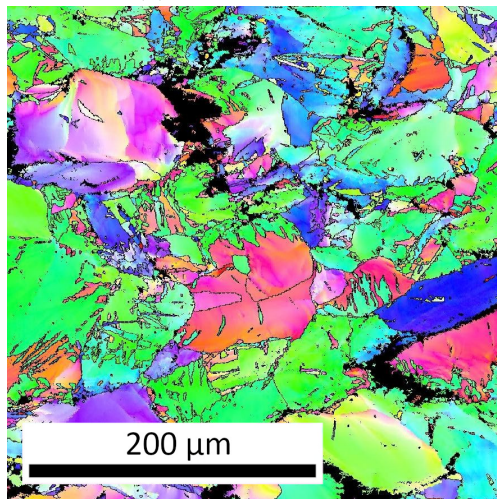
(d) 10 % eng. strain
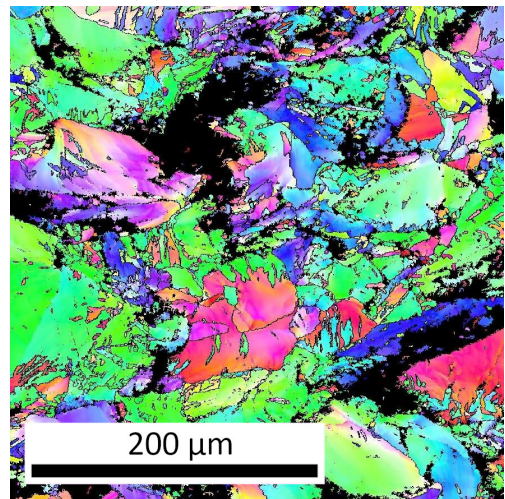
(e) 20 % eng. strain

(f) 30 % eng. strain

Figure 3.28: Orientation maps acquired using EBSD during interrupted deformation experiment on the sample co1100-20c.
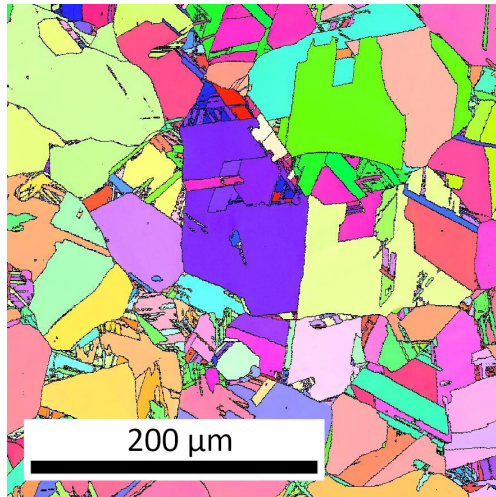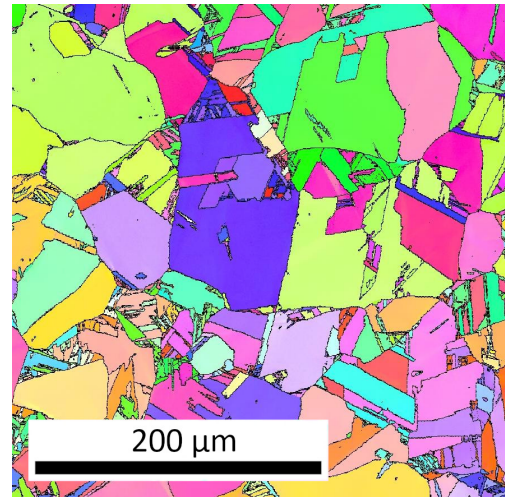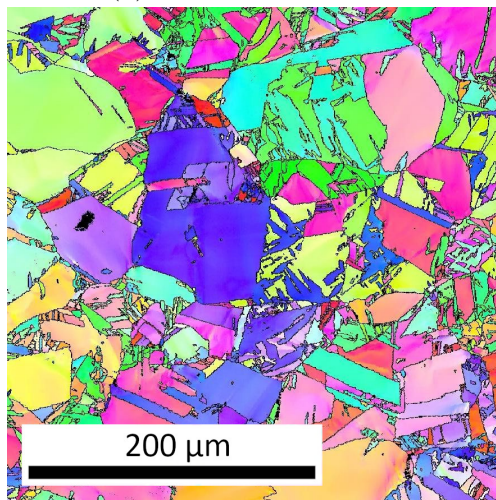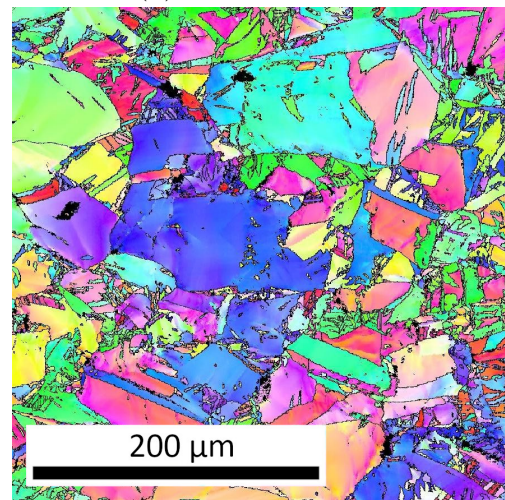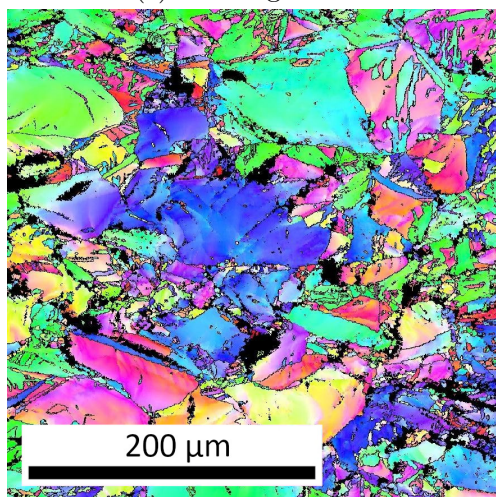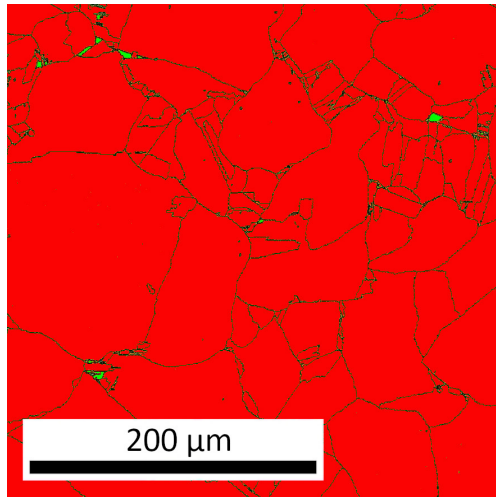
(a) Before deformation
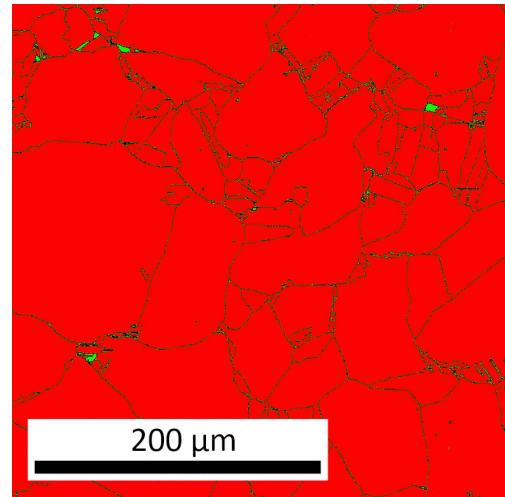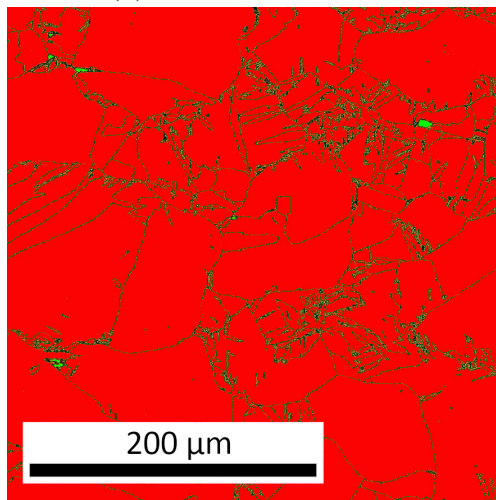
(b) 1 % eng. strain
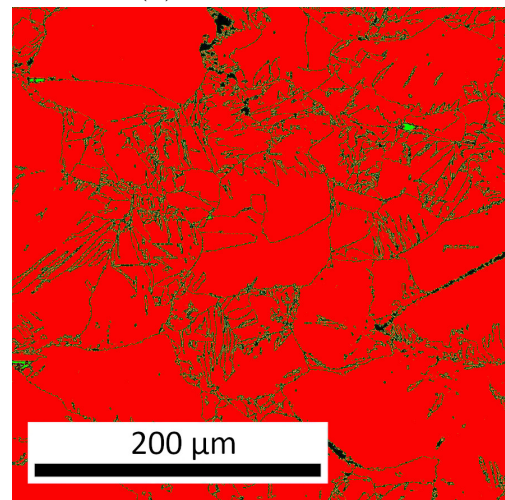
(c) 4 % eng. strain
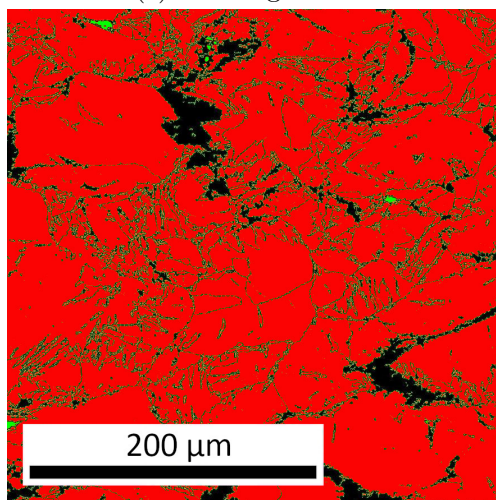
(d) 10 % eng. strain
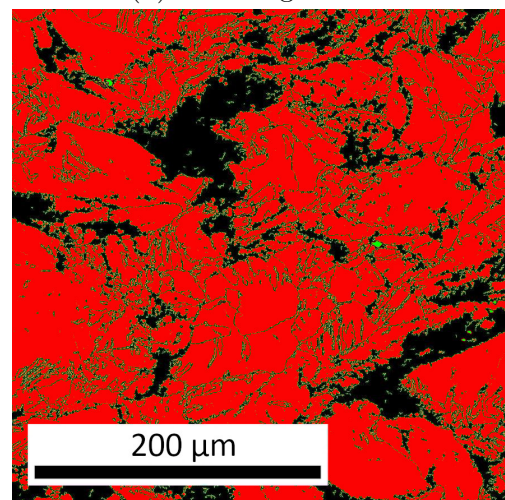
(e) 20 % eng. strain

(f) 30 % eng. strain

Figure 3.29: Phase maps extracted from EBSD acquired during interrupted deformation experiment on the sample co1100-20c.
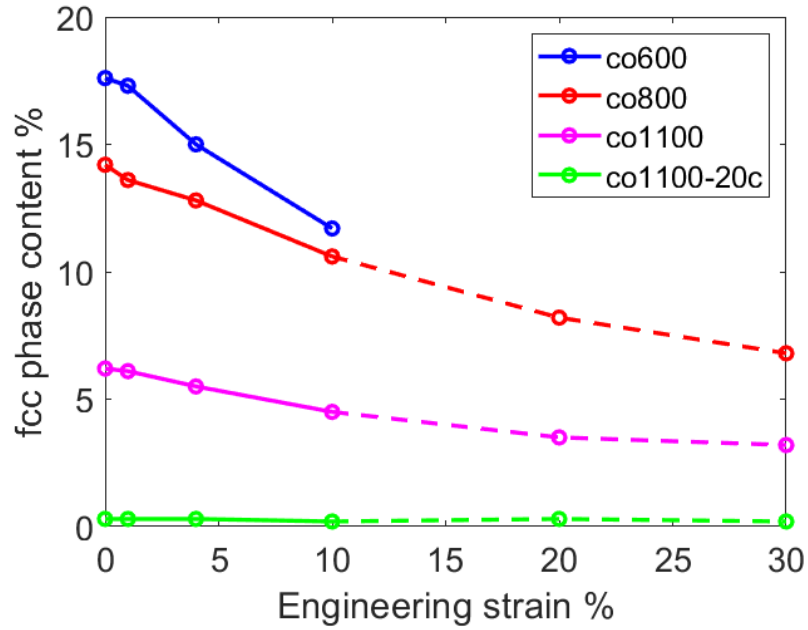
Figure 3.30: Evolution of fcc phase content during interrupted deformation experiment. Values recorded for 20 % and 30 % have to be viewed with caution as the number of low CI points increases significantly.
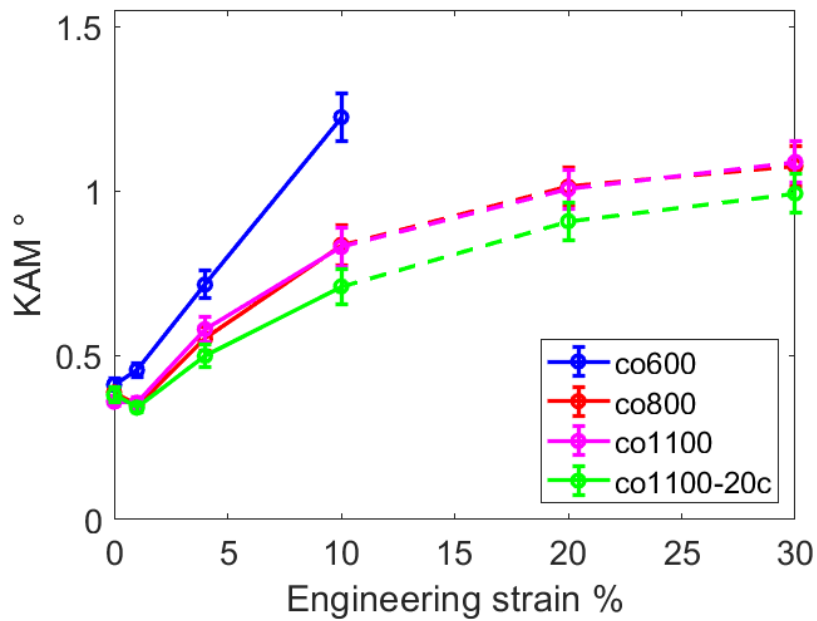
Figure 3.31: Evolution of KAM during interrupted deformation experiment. Values recorded for 20 % and 30 % have to be viewed with caution as the number of low CI points increases significantly.
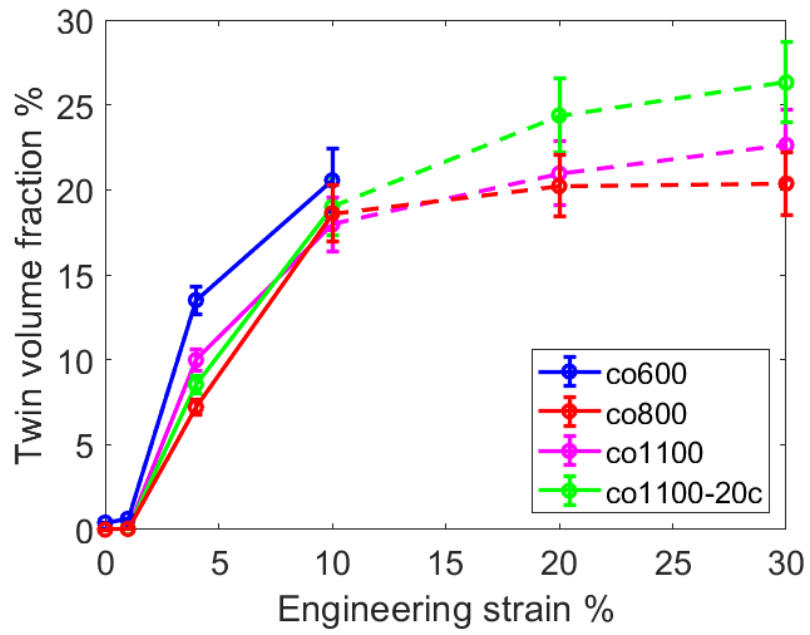
Figure 3.32: Evolution of twin volume fraction during interrupted deformation experiment. Values recorded for 20 % and 30 % have to be viewed with caution as the number of low CI points increases significantly.

4. Discussion

The deformation tests described in Section 3.2 show a clear dependence of $\sigma_{0.2}$ on annealing temperature in samples not subjected to thermal cycling. This inverse proportion can be explained by the well know Hall-Petch (HP) relation [72], which states that $\sigma_{0.2}$ is proportional to the inverse of the square root of grain size $d^{-\frac{1}{2}}$. As grain size becomes normalised independent of previous annealing temperature after thermal cycling, so does this relation stop influencing the observed $\sigma_{0.2}$. This behaviour has been observed in cobalt before [26, 73]. In both the sets of samples that were subjected to thermal cycling the further grain growth makes the grain size fall to a narrower range and in the case of twenty cycles effectively erases the previous thermal treatment dependence. With the variance in grain size absent, the values of $\sigma_{0.2}$ seem to only slightly fluctuate in these sets without a clear dependence on the small differences in grain size present. The value of ε_{max} seems to increase for samples co600, co700, co800 and co900 with higher annealing temperature and then does not change significantly for samples co900, co1000, co1100. Likely explanation is recrystallization, which is accelerated by higher annealing temperature. Complete recrystallization is apparently achieved after annealing at 900 °C and higher temperature annealing does not significantly change the value of ε_{max}.

After thermal cycling the values of ε_{max} and σ_{max} drop significantly. This may be explained as the influence of reduced residual fcc phase. While the transformation from fcc to hcp brings about only about $\approx 0.4\%$ volume change, the abundance of slip systems present in the fcc structure can accommodate a significant shape change of the fcc grains [16]. This is supported by the interrupted deformation tests. As shown in Figure 4.1 the fcc grains seem to severely change shape over the course of deformation, while transformation into hcp seems more gradual. At the same time the presence of the fcc phase can increase σ_{max} as the presence of intersecting slip planes leads to more strain hardening compared to the hcp phase [74].

There is another slight decrease in ε_{max} observed between the samples subjected to ten and twenty thermal cycles, in spite of the fact that already after ten cycles the fcc phase was shown to be mostly eliminated (Table 3.1). It has been shown before that larger grain size in hcp materials can cause twinning to be more easily activated [68, 75]. The high angle boundaries introduced by the twinning then present new barriers to slip. This may contribute to the decrease in ductility in hcp materials with larger grains [76, 77]. On the other hand higher twinned volume can present more opportunity for easy basal slip as the crystal orientation changes during twinning. This contributes to an opposite effect of increasing ε_{max} [78]. However the interrupted deformation tests show only a minor increase in the twinned volume in co1100-20c compared to the annealed samples. At the same time microstructure observations presented in Table 3.1 do not show a significant increase in grain size between sample types co1100-10c and co1100-20c. While the first ten cycles were shown to already mostly eliminate residual fcc phase, the DSC and TD data shown in Figure 2.2 suggest a further evolution of the transformation between ten and twenty cycles. This is connected to the evolution of transformation shown in Figure 1.4. The further transforma-
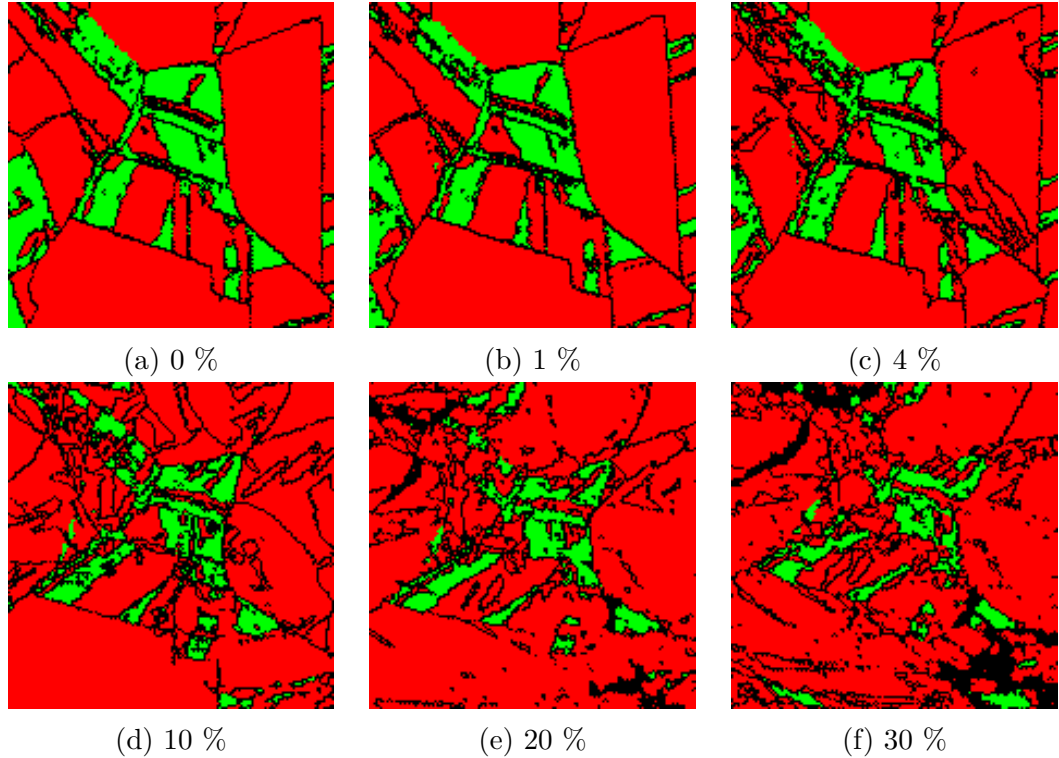
Figure 4.1: A close up from the co800 phase maps of a region containing fcc grains and its evolution during deformation. Red colour is hcp, green is fcc. A compressive load is being applied in a direction parallel with the map plane, vertical in respect to the page. A percentage of engineering strain is noted under every step. The fcc grains visibly change shape while only partially transforming.

tion evolution results in reorganisation of dislocation arrays that take part in the transformation as well as the evolution of the size and shape of hcp grains after transformation [40]. Consequently, such an advancing evolution of the fcc phase microstructure can influence the deformation dynamics, including the $\varepsilon_{\max}$ value.

Additional information about the deformation is provided by the results of interrupted deformation. The EBSD maps show activation of twinning. In samples co600, co1100 and co1100-20c only the $\{10\bar{1}2\}$ extension twin type, which is the easiest to activate, is observed. The sample co800 also contains $\{11\bar{2}1\}$ type twinning. These twins appear in a "zig-zag" pattern inside the parent grain as can be seen in Figure 4.2. This was also observed in [46]. Once these twins nucleate, they do not seem to grow significantly during the remainder of the experiment. The $\{11\bar{2}1\}$ type twinning has a significantly higher CRSS compared to $\{10\bar{1}2\}$ type twinning, although it has been observed before [46, 47]. It is unclear why only this sample shows activation of this twinning mode and not the others. An important factor could be the local nature of EBSD which covers only a small surface area as opposed to the full volume of the sample. The $\{11\bar{2}1\}$ twins could just be out of the observed area on all the other samples. Counter to that is the fact that the $\{11\bar{2}1\}$ twins are observed in three separate grains within the EBSD area, suggesting they might not be quite as rare. Comparing the microstructure of all the samples observed in interrupted deformation and also the samples used in [46] and [47], there does not seem to be a clear link to a specific microstructure

either. Additionally to the special twin boundaries many grain boundaries in hcp have a 71° misorientation as can be seen in Figure 4.2. This is the result of one fcc grain transforming into multiple hcp grains as is described in Section 1.2. The 71° misorientation angle is a result of Shoji-Nishiyama geometric relation [45] between these grains. While the DSC and TD measurements in Figure 2.2 suggest a stabilisation of the transformation and the transformation temperatures converging to constant values, the presence of the 71° boundaries even in the sample co1100-20c suggests the transformation is not yet fully stabilised and reversible even after twenty cycles. It does seem however that even this partial stabilisation is enough for all or almost all fcc phase to transform into hcp upon cooling. As mentioned above, this continuing evolution of the transformation is likely linked to the observed change in the values of ε_{max} and σ_{max} between 10c and 20c samples. As suggested in [40] further cycling should lead to these special boundaries disappearing and the transformation evolving toward the ideal state of one fcc grain transforming into one hcp grain. As some hcp grains become bigger during this stabilisation pushing the smaller ones out a bimodal microstructure of growing and shrinking grains may arise.

The twinned fraction evolution during deformation follows a pattern of fast increase caused by nucleation up to 10% deformation followed by slower increase, when twin nucleation is exhausted and only twin growth occurs. In all samples some twins are observed to nucleate already at the 1 % point, which is still within the elastic phase of deformation. This suggest, together with AE data, that some irreversible plastic changes take place before $\sigma_{0.2}$. It would thus be more accurate to use the term quasi-elastic deformation. The measurements of KAM however do not support the presence of significant dislocation activity during this quasi-elastic phase, counter to the AE observations, which may thus reflect solely the twinning activity. Further evolution of KAM during the remainder of deformation shows an increase in dislocation density. This increase slows down as deformation progresses and dislocation mobility decreases in the more deformed sample.

The interrupted deformation experiment shows that the evolution of twin volume fraction during deformation fits well to the observed AE signal. During the part of deformation where the amplitudes of AE events are high the twin volume fraction is increasing fast and the maps show new twins nucleating. After this the AE is reduced to low amplitude sporadic signals. At the same time the EBSD shows mainly further growth of existing twins, which is known to be a very weak source of AE [49]. The fcc fraction on the other hand continues to decrease beyond the region of deformation in which AE is active. This observation testifies that the transformation process might be, indeed, sluggish (at least at the conditions used in these experiments). The EBSD data seem to support this, as the fcc grains seem to gradually decrease in size during deformation. An example of this can be seen in detail in Figure 4.1. These observations suggest that the transformation is incremental and thus a weak source of AE. The KAM observation suggest the dislocation density evolution does not slow down as much beyond the point when AE activity mostly disappears. The increase in KAM in later stages of deformation could be linked to higher number of smaller avalanches within the already deformed microstructure that fall under the threshold of AE. A slight disparity between the interrupted deformation experiment and AE appears in the quasi-elastic part of deformation or more precisely between the 0% and 1%

(a) co800

(b) co800

(c) co1100-20c
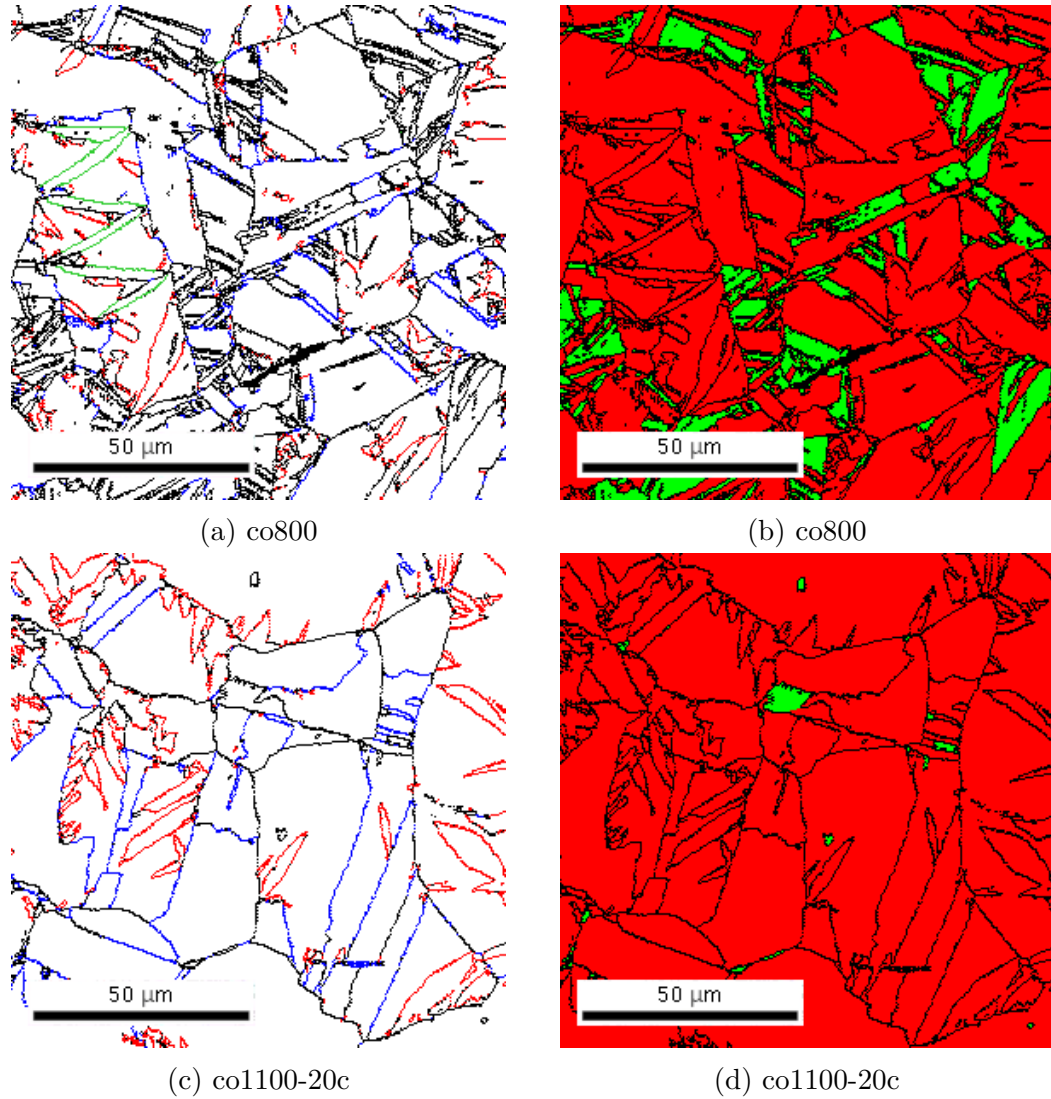
(d) co1100-20c

Figure 4.2: Details of grain boundaries. Figure (a) shows a close up of an area on the sample co800 at the 4 % engineering strain point. Figure (b) shows the phase map of that area. Figure (c) shows a close up of an area on the sample co1100-20c at the 4 % engineering strain point. Note that after twenty cycles there are still 71° boundaries present. Figure (d) again shows the phase map of that area. Red lines are $\{10\bar{1}2\}$ twin boundaries, green lines are $\{11\bar{2}1\}$ twin boundaries and blue lines are 71° misorientation boundaries. On phase maps red is hcp and green is fcc.
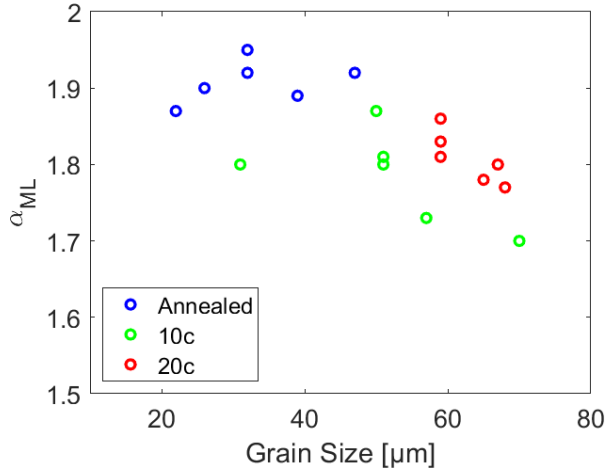
Figure 4.3: The α_{ML} coefficient plotted against grain size.

deformation points in interrupted deformation. While some twin nucleation is observed to take place, the measured KAM and twin volume fraction would suggest overall small extent of activated deformation mechanisms. The amplitudes of AE events on the other hand are rather high suggesting high energy of the events taking place. The microstructure at this point contains few dislocations and twin boundaries, presenting less barriers that would limit the size of the events. This quasi-elastic stage of deformation has been observed before in hcp metals [79].

The α_{ML} coefficient observed in distributions of A^2 of AE events in annealed samples ranges from ≈ 1.87 to ≈ 1.95, which is somewhat at the high end or above the generally reported range of 1.5 to 1.8 [55, 58]. Although exponents as high as 2 have been reported in the plastic deformation of single crystals [59]. The α_{ML} coefficient observed in samples subjected to thermal cycling ranges from ≈ 1.70 to ≈ 1.87 for both ten and twenty cycles. A possible explanation for the change would be that the larger grains with significantly less fcc grains acting as barriers allow for higher probability of larger dislocation avalanches and nucleation of larger twins [63, 70]. Figure 4.3 shows a plot of α_{ML} values plotted against grain size. There seems to be a relation between the α_{ML} coefficient and grain size, but it is rather weak. More measurements across a wider variety of grain size and fcc phase fraction values might be necessary to fully interpret this relation. Nonetheless, these results confirm the presence of power law statistics in AE events in compressive deformation of pure polycrystalline cobalt across many orders of magnitude. The observed change in α_{ML} after thermal cycling and almost completed reduction in fcc phase fraction is of special interest. Previous studies have shown dependence of α coefficient on microstructure in polycrystalline materials, mainly focusing on grain size [63]. Influencing the α coefficient via the fcc phase fraction in cobalt presents a new avenue for studying SOC phenomena in polycrystalline materials.

Conclusion

Samples of pure polycrystalline cobalt prepared under different conditions with the aim of creating a diverse set of microstructures were investigated using EBSD and were further subjected to deformation testing combined with the AE technique. The AE data were tested for the presence of power law probability distributions. Additionally selected samples were investigated by the means of semi in-situ interrupted deformation experiments combined with EBSD. The EBSD acquired during interrupted deformation was further used to determine fcc fraction, KAM and twin volume fraction at every deformation step. This combination of experiments was chosen with the goal of gaining deeper insight into the elementary mechanisms that accommodate plastic deformation in cobalt and how they act during compressive deformation. The conclusions drawn from these experiments are as follows:

- The general dependence of deformation behaviour on grain size observed during deformation is in line with what is expected in hcp metals. Additionally the presence of fcc grains influences the deformation significantly. The abundance of slip systems in the fcc structure compared to hcp allow the fcc grains to accommodate significant shape change, enhancing the hardening and ductility of the material.

- While retained fcc phase might increase strength and ductility, the amount of fcc phase the material retains at room temperature seems to be dependent on many factors and engineering a material with a predictable fcc fraction might be a challenge. Thermally cycling the samples does stabilise the phase transformation. Even then further EBSD investigation show that material where the fcc phase transforms completely has not yet reached fully stable transformation after twenty thermal cycles through the transformation temperature. The presence of 71° misorientation boundaries observed in this work confirms that the transformation further evolves. This evolution also involves some grains in hcp growing at the expense of smaller grains with further thermal cycling. Creating a procedure that would form a perfectly predictable and adjustable microstructure in cobalt still remains a challenge. Further experiments using perhaps a chain of multiple annealing and thermal cycling procedures might be necessary.

- Martensitic transformation in general is considered a rather strong source of AE. However the transformation present in pure cobalt is shown to happen gradually during deformation without the sudden transition of phases in larger regions that would be a strong source of AE. A significant fraction of fcc is even retained in the material all the way up to fracture. Hence, while stress induced martensitic transformation is observed it is rather sluggish and likely not the main contribution of fcc phase to deformation.

- The distribution of A^2 of events measured in AE signal in annealed samples follow a power law, but with a coefficient which is at or slightly above the high end of what is observed in plastic deformation of polycrystalline metals. The coefficient slightly decreases after the elimination of residual fcc phase,

suggesting possible connection to the presence of fcc phase and the hcp phase grain size. Further experiments involving more samples of different microstructures and additional techniques, such as interrupted deformation with more steps, in-situ TEM, in-situ XRD or analysing AE signals in the frequency domain might be able to better explain the observed phenomena. This presents a new opportunity for the study of correlated dislocation dynamics.

- The combination of unique properties present in cobalt make it an interesting subject of study. The results presented in this work expand the rather limited existing body of work on pure cobalt and its deformation behaviour. Further understanding of the fine details of how different deformation mechanisms and the martensitic transformation influence each other is crucial to reach a deeper understanding of deformation in cobalt and hcp metals in general.

Bibliography

1. KITTEL, C. *Introduction to Solid State Physics*. 8th ed. Hoboken, New Jersey, USA: John Wiley & Sons, 2005. ISBN 0-471-41526-X.

2. KUBIN, L. P. Dislocation Patterning during Multiple Slip of F.C.C. Crystals. A Simulation Approach. *Physica Status Solidi A*. 1993, vol. 135, no. 2, pp. 433–443. Available from DOI: `10.1002/pssa.2211350209`.

3. KONEVA, N.A.; KOZLOV, E.V.; TRISHKINA, L.I.; PEKARSKAYA, E.E. Thermodynamics of substructure transformations under plastic deformation of metals and alloys. *Materials Science and Engineering: A*. 1997, vol. 234-236, pp. 614–616. ISSN 0921-5093. Available from DOI: `10.1016/S0921-5093(97)00271-2`.

4. WEISS, J.; RICHETON, T.; LOUCHET, F.; CHMELÍK, F.; DOBROŇ, P.; ENTEMEYER, D.; LEBYODKIN, M.; LEBEDKINA, T. A.; FRESSENGEAS, C.; MCDONALD, R. J. Evidence for universal intermittent crystal plasticity from acoustic emission and high-resolution extensometry experiments. *Physical Review B*. 2007, vol. 76, p. 224110. Available from DOI: `10.1103/PhysRevB.76.224110`.

5. SHASHKOV, I. *Multiscale study of the intermittency of plastic deformation by acoustic emission method*. 2012. PhD thesis. Université de Lorraine.

6. MIGUEL, M. C.; VESPIGNANI, A.; ZAPPERI, S.; WEISS, J.; GRASSO, J. R. Intermittent dislocation flow in viscoplastic deformation. *Nature*. 2001, vol. 410, no. 6829, pp. 667–671. ISSN 1476-4687. Available from DOI: `10.1038/35070524`.

7. BAK, P.; TANG, C.; WIESENFELD, K. Self-organized criticality: An explanation of the 1/f noise. *Physical Review Letters*. 1987, vol. 59, pp. 381–384. Available from DOI: `10.1103/PhysRevLett.59.381`.

8. KIANI, M.; GANDIKOTA, I.; RAIS-ROHANI, M.; MOTOYAMA, K. Design of lightweight magnesium car body structure under crash and vibration constraints. *Journal of Magnesium and Alloys*. 2014, vol. 2, no. 2, pp. 99–108. ISSN 2213-9567. Available from DOI: `10.1016/j.jma.2014.05.005`.

9. BERTHOD, P. High-Temperature Extreme Alloys. In: CABALLERO, F. G. (ed.). *Encyclopedia of Materials: Metals and Alloys*. Oxford: Elsevier, 2022, pp. 311–322. ISBN 978-0-12-819733-2. Available from DOI: `10.1016/B978-0-12-803581-8.12074-0`.

10. CAMPBELL, F.C. *Elements of Metallurgy and Engineering Alloys*. ASM International, 2008. ISBN 9781615030583.

11. WILSON, J. 1 - Metallic biomaterials: State of the art and new challenges. In: BALAKRISHNAN, P.; SREEKALA, M. S.; SABU, T. (eds.). *Fundamental Biomaterials: Metals*. Woodhead Publishing, 2018, pp. 1–33. Woodhead Publishing Series in Biomaterials. ISBN 978-0-08-102205-4. Available from DOI: `10.1016/B978-0-08-102205-4.00001-5`.

12. TANZI, M. C.; FARÈ, S.; CANDIANI, G. Chapter 4 - Biomaterials and Applications. In: *Foundations of Biomaterials Engineering.* Academic Press, 2019, pp. 199–287. ISBN 978-0-08-101034-1. Available from DOI: `10.1016/B978-0-08-101034-1.00004-9`.

13. DISEGI, J.A.; KENNEDY, R.L.; PILLIAR, R. *Cobalt-base Alloys for Biomedical Applications.* ASTM, 1999. STP 1365. ISBN 9780803126084.

14. ZHENG, G. P. Grain-size effect on plastic flow in nanocrystalline cobalt by atomistic simulation. *Acta Materialia.* 2007, vol. 55, no. 1, pp. 149–159. ISSN 1359-6454. Available from DOI: `10.1016/j.actamat.2006.07.034`.

15. CRONE, W. C. A Brief Introduction to MEMS and NEMS. In: *Springer Handbook of Experimental Solid Mechanics.* Ed. by SHARPE, W. N. Boston, MA: Springer US, 2008, pp. 203–228. ISBN 978-0-387-30877-7. Available from DOI: `10.1007/978-0-387-30877-7_9`.

16. SANDERSON, C. C. *Deformation of polycrystalline cobalt.* 1972. Available from DOI: `10.14288/1.0078728`. PhD thesis. University of British Columbia.

17. BETTERIDGE, W. The properties of metallic cobalt. *Progress in Materials Science.* 1980, vol. 24, pp. 51–142. ISSN 0079-6425. Available from DOI: `10.1016/0079-6425(79)90004-5`.

18. DUBOS, P.-A.; FAJOUI, J.; ISKOUNEN, N.; CORET, M.; KABRA, S.; KELLEHER, J.; GIRAULT, B.; GLOAGUEN, D. Temperature effect on strain-induced phase transformation of cobalt. *Materials Letters.* 2020, vol. 281, p. 128812. ISSN 0167-577X. Available from DOI: `10.1016/j.matlet.2020.128812`.

19. HOLT, R. T. *The high temperature deformation of cobalt single crystals.* 1968. PhD thesis. The University of British Columbia.

20. SEEGER, A.; KRONMÜLLER, H.; BOSER, O.; RAPP, M. Plastische Verformung von Kobalteinkristallen. *Physica Status Solidi B.* 1963, vol. 3, no. 6, pp. 1107–1125. Available from DOI: `10.1002/pssb.19630030617`.

21. MARX, V.M.; KIRCHLECHNER, C.; BREITBACH, B.; CORDILL, M.J.; TÖBBENS, D.M.; WAITZ, T.; DEHM, G. Strain-induced phase transformation of a thin Co film on flexible substrates. *Acta Materialia.* 2016, vol. 121, pp. 227–233. ISSN 1359-6454. Available from DOI: `10.1016/j.actamat.2016.09.015`.

22. SORT, J.; NOGUÉS, J.; SURIÑACH, S.; BARÓ, M. D. Microstructural aspects of the hcp-fcc allotropic phase transformation induced in cobalt by ball milling. *Philosophical Magazine.* 2003, vol. 83, no. 4, pp. 439–455. Available from DOI: `10.1080/0141861021000047159`.

23. EDALATI, K.; TOH, S.; ARITA, M.; WATANABE, M.; HORITA, Z. High-pressure torsion of pure cobalt: hcp-fcc phase transformations and twinning during severe plastic deformation. *Applied Physics Letters.* 2013, vol. 102, no. 18, p. 181902. ISSN 0003-6951. Available from DOI: `10.1063/1.4804273`.

24. BARRY, A. H.; DIRRAS, G.; SCHOENSTEIN, F.; TÉTARD, F.; JOUINI, N. Microstructure and mechanical properties of bulk highly faulted fcc/hcp nanostructured cobalt microstructures. *Materials Characterization.* 2014, vol. 91, pp. 26–33. ISSN 1044-5803. Available from DOI: `10.1016/j.matchar.2014.02.004`.

25. ZHU, Y.T.; ZHANG, X.Y.; LIU, Q. Observation of twins in polycrystalline cobalt containing face-center-cubic and hexagonal-close-packed phases. *Materials Science and Engineering: A.* 2011, vol. 528, no. 28, pp. 8145–8149. ISSN 0921-5093. Available from DOI: `10.1016/j.msea.2011.07.062`.

26. FLEURIER, G.; HUG, E.; MARTINEZ, M.; DUBOS, P. A.; KELLER, C. Size effects and Hall–Petch relation in polycrystalline cobalt. *Philosophical Magazine Letters.* 2015, vol. 95, no. 2, pp. 122–130. Available from DOI: `10.1080/09500839.2015.1020351`.

27. MARTINEZ, M.; FLEURIER, G.; CHMELÍK, F.; KNAPEK, M.; VIGUIER, B.; HUG, E. TEM analysis of the deformation microstructure of polycrystalline cobalt plastically strained in tension. *Materials Characterization.* 2017, vol. 134, pp. 76–83. ISSN 1044-5803. Available from DOI: `10.1016/j.matchar.2017.09.038`.

28. GOTTSTEIN, G. *Physical foundations of materials science.* 1st ed. New York: Springer-Verlag Berlin Heidelberg, 2004. ISBN 978-3-540-40139-1. Available from DOI: `10.1007/978-3-662-09291-0`.

29. SCHMID, E; BOAS, W. *Plasticity of Crystals with Special Reference to Metals.* 1st ed. London: Hughes & Co., 1950.

30. TAYLOR, G. I. Plastic strain in metals. *Journal of the Institute of Metals.* 1938, vol. 62, pp. 307–324.

31. MISES, R. V. Mechanik der plastischen Formänderung von Kristallen. *ZAMM - Journal of Applied Mathematics and Mechanics / Zeitschrift für Angewandte Mathematik und Mechanik.* 1928, vol. 8, no. 3, pp. 161–185. Available from DOI: `10.1002/zamm.19280080302`.

32. PARTRIDGE, P. G. The crystallography and deformation modes of hexagonal close-packed metals. *Metallurgical Reviews.* 1967, vol. 12, no. 1, pp. 169–194. Available from DOI: `10.1179/mtlr.1967.12.1.169`.

33. YOSHINAGA, H.; HORIUCHI, R. Deformation Mechanisms in Magnesium Single Crystals Compressed in the Direction Parallel to Hexagonal Axis. *Transactions of the Japan Institute of Metals.* 1963, vol. 4, no. 1, pp. 1–8. Available from DOI: `10.2320/matertrans1960.4.1`.

34. CHINO, Y.; KIMURA, K.; HAKAMADA, M.; MABUCHI, M. Mechanical anisotropy due to twinning in an extruded AZ31 Mg alloy. *Materials Science and Engineering: A.* 2008, vol. 485, no. 1, pp. 311–317. ISSN 0921-5093. Available from DOI: `10.1016/j.msea.2007.07.076`.

35. XU, S.; TOTH, L. S.; SCHUMAN, C.; LECOMTE, J. S.; BARNETT, M. R. Dislocation mediated variant selection for secondary twinning in compression of pure titanium. *Acta Materialia.* 2017, vol. 124, pp. 59–70. ISSN 1359-6454. Available from DOI: `10.1016/j.actamat.2016.10.063`.

36. ARUL KUMAR, M.; WROŃSKI, M.; MCCABE, R.J.; CAPOLUNGO, L.; WIERZBANOWSKI, K.; TOMÉ, C.N. Role of microstructure on twin nucleation and growth in HCP titanium: A statistical study. *Acta Materialia.* 2018, vol. 148, pp. 123–132. ISSN 1359-6454. Available from DOI: `10.1016/j.actamat.2018.01.041`.

37. BINGERT, J. R.; MASON, T. A.; KASCHNER, G. C.; GRAY, G. T.; MAUDLIN, P. J. Deformation twinning in polycrystalline Zr: Insights from electron backscattered diffraction characterization. *Metallurgical and Materials Transactions A.* 2002, vol. 33, no. 3, pp. 955–963. ISSN 1543-1940. Available from DOI: `10.1007/s11661-002-0165-7`.

38. ALDINGER, F. Flow and fracture of single crystals (beryllium crystal dislocations). *Beryllium science and technology.* 1979, vol. 1, pp. 7–114.

39. RAVI KUMAR, N.V; BLANDIN, J.J; DESRAYAUD, C; MONTHEILLET, F; SUÉRY, M. Grain refinement in AZ91 magnesium alloy during thermomechanical processing. *Materials Science and Engineering: A.* 2003, vol. 359, no. 1, pp. 150–157. ISSN 0921-5093. Available from DOI: `10.1016/S0921-5093(03)00334-4`.

40. BAUER, R.; JÄGLE, E. A.; BAUMANN, W.; MITTEMEIJER, E. J. Kinetics of the allotropic hcp–fcc phase transformation in cobalt. *Philosophical Magazine.* 2011, vol. 91, no. 3, pp. 437–457. Available from DOI: `10.1080/14786435.2010.525541`.

41. MUNIER, A.; BIDAUX, J. E.; SCHALLER, R.; ESNOUF, C. Evolution of the microstructure of cobalt during diffusionless transformation cycles. *Journal of Materials Research.* 1990, vol. 5, no. 4, pp. 769–775. ISSN 2044-5326. Available from DOI: `10.1557/JMR.1990.0769`.

42. BIDAUX, J. E.; SCHALLER, R.; BENOIT, W. Study of the hcp-fcc phase transition in cobalt by internal friction and elastic modulus measurements in the kHz frequency range. *Journal de Physique Colloques.* 1987, vol. 48, pp. C8477–C8482. Available from DOI: `10.1051/jphyscol:19878741`.

43. KUANG, Z.Q; ZHANG, J.X; ZHANG, X.H; LIANG, K.F; FUNG, P.C.W. Latent heat in the thermoelastic martensitic transformation of Co. *Scripta Materialia.* 2000, vol. 42, no. 8, pp. 795–799. ISSN 1359-6462. Available from DOI: `10.1016/S1359-6462(00)00297-9`.

44. VOTAVA, E. Electron microscopic investigation of the phase transformation of thin cobalt samples. *Acta Metallurgica.* 1960, vol. 8, no. 12, pp. 901–904. ISSN 0001-6160. Available from DOI: `10.1016/0001-6160(60)90166-8`.

45. MORRIS, E. F.; MESHII, M.; WAYMAN, C. M.; NISHIYAMA, Z. (eds.). 2 - Crystallography of Martensite (General). In: *Martensitic Transformation.* Academic Press, 1978, pp. 14–134. ISBN 978-0-12-519850-9. Available from DOI: `10.1016/B978-0-12-519850-9.50007-7`.

46. MARTINEZ CELIS, M.; MINÁRIK, P.; HUG, E.; DORENLOR, J., et al. Analysis of the twin variant selection in polycrystalline cobalt. *Journal of Materials Science.* 2021, vol. 56, pp. 7740–7752. Available from DOI: `10.1007/s10853-020-05718-9`.

47. ZHANG, X.Y.; ZHU, Y.T.; LIU, Q. Deformation twinning in polycrystalline Co during room temperature dynamic plastic deformation. *Scripta Materialia.* 2010, vol. 63, no. 4, pp. 387–390. ISSN 1359-6462. Available from DOI: `10.1016/j.scriptamat.2010.04.031`.

48. HEIPLE, C. R.; CARPENTER, S. H.; THOMAS, R. L. Acoustic emission produced by deformation of metals and alloys. *Journal of Acoustic Emission.* 1987, vol. 6, no. 2. Available from DOI: `10.2172/6230904`.

49. MÁTHIS, K.; CHMELÍK, F. Exploring Plastic Deformation of Metallic Materials by the Acoustic Emission Technique. In: SIKORSKI, W. (ed.). *Acoustic Emission.* Rijeka: IntechOpen, 2012, chap. 2. Available from DOI: `10.5772/31660`.

50. HATANO, H. Quantitative measurements of acoustic emission related to its microscopic mechanisms. *Journal of the Acoustical Society of America.* 1975, vol. 57, pp. 639–645.

51. CLAUSET, A.; SHALIZI, C. R.; NEWMAN, M. E. J. Power-Law Distributions in Empirical Data. *SIAM Review.* 2009, vol. 51, no. 4, pp. 661–703. Available from DOI: `10.1137/070710111`.

52. MUNIRUZZAMAN, A. N. M. On Measures of Location and Dispersion and Tests of Hypotheses in a Pare to Population. *Calcutta Statistical Association Bulletin.* 1957, vol. 7, no. 3, pp. 115–123. Available from DOI: `10.1177/0008068319570303`.

53. CLAUSET, A.; YOUNG, M.; GLEDITSCH, K. S. On the Frequency of Severe Terrorist Events. *Journal of Conflict Resolution.* 2007, vol. 51, no. 1, pp. 58–87. Available from DOI: `10.1177/0022002706296157`.

54. PRESS, W. H.; TEUKOLSKY, S. A.; VETTERLING, W. T.; FLANNERY, B. P. *Numerical Recipes in C: The Art of Scientific Computing.* 2nd ed. Cambridge, England: Cambridge University Press, 1992. ISBN 0-521-43108-5.

55. WEISS, J.; GRASSO, J. R. Acoustic Emission in Single Crystals of Ice. *Journal of Physical Chemistry B.* 1997, vol. 101. Available from DOI: `10.1021/jp963157f`.

56. ESHELBY, J. D.; RAYNOR, G. V. The interaction of kinks and elastic waves. *Proceedings of the Royal Society of London. Series A. Mathematical and Physical Sciences.* 1962, vol. 266, no. 1325, pp. 222–246. Available from DOI: `10.1098/rspa.1962.0058`.

57. RICHETON, T.; WEISS, J.; LOUCHET, F. Dislocation avalanches: Role of temperature, grain size and strain hardening. *Acta Materialia.* 2005, vol. 53, no. 16, pp. 4463–4471. ISSN 1359-6454. Available from DOI: `10.1016/j.actamat.2005.06.007`.

58. WEISS, J; GRASSO, J R; MIGUEL, M. C.; VESPIGNANI, A; ZAPPERI, S. Complexity in dislocation dynamics: experiments. *Materials Science and Engineering: A.* 2001, vol. 309-310, pp. 360–364. ISSN 0921-5093. Available from DOI: `10.1016/S0921-5093(00)01633-6`.

59. WEISS, J.; RHOUMA, W. B.; RICHETON, T.; DECHANEL, S., et al. From Mild to Wild Fluctuations in Crystal Plasticity. *Phys. Rev. Lett.* 2015, vol. 114, p. 105504. Available from DOI: `10.1103/PhysRevLett.114.105504`.

60. RICHETON, T.; WEISS, J.; LOUCHET, F.; DOBROŇ, P.; CHMELÍK, F. Critical character of plasticity from AE experiments in hcp and fcc metals. *Kovove Materialy.* 2007, vol. 45, pp. 149–152. ISSN 1338-4252.

61. ZAISER, M. Scale invariance in plastic flow of crystalline solids. *Advances in Physics.* 2006, vol. 55, no. 1-2, pp. 185–245. Available from DOI: `10.1080/00018730600583514`.

62. RICHETON, T.; WEISS, J.; LOUCHET, F. Breakdown of avalanche critical behaviour in polycrystalline plasticity. *Nature Materials.* 2005, vol. 4, pp. 465–469. Available from DOI: `10.1038/nmat1393`.

63. WEISS, J. Ice: the paradigm of wild plasticity. *Philosophical Transactions of the Royal Society A: Mathematical, Physical and Engineering Sciences.* 2019, vol. 377, no. 2146, p. 20180260. Available from DOI: `10.1098/rsta.2018.0260`.

64. LEBYODKIN, M.; KOBELEV, N. P.; BOUGHERIRA, Y.; ENTEMEYER, D.; FRESSENGEAS, C.; LEBEDKINA, Ta. A.; SHASHKOV, I. V. On the similarity of plastic flow processes during smooth and jerky flow in dilute alloys. *Acta Materialia.* 2012, vol. 60, pp. 844–850. ISSN 1359-6454. Available from DOI: `10.1016/j.actamat.2011.10.042`.

65. BOUGHERIRA, Y; ENTEMEYER, D; FRESSENGEAS, C; KOBELEV, N P; LEBEDKINA, T A; LEBYODKIN, M A. The intermittency of plasticity in an Al 3 % Mg alloy. *Journal of Physics: Conference Series.* 2010, vol. 240, no. 1, p. 012009. Available from DOI: `10.1088/1742-6596/240/1/012009`.

66. CALCAGNOTTO, M.; PONGE, D.; DEMIR, E.; RAABE, D. Orientation gradients and geometrically necessary dislocations in ultrafine grained dual-phase steels studied by 2D and 3D EBSD. *Materials Science and Engineering: A.* 2010, vol. 527, no. 10, pp. 2738–2746. ISSN 0921-5093. Available from DOI: `10.1016/j.msea.2010.01.004`.

67. KUBIN, L.P; MORTENSEN, A. Geometrically necessary dislocations and strain-gradient plasticity: a few critical issues. *Scripta Materialia.* 2003, vol. 48, no. 2, pp. 119–125. ISSN 1359-6462. Available from DOI: `10.1016/S1359-6462(02)00335-4`.

68. DOBROŇ, P.; CHMELÍK, F.; YI, S.; PARFENENKO, K.; LETZIG, D.; BOHLEN, J. Grain size effects on deformation twinning in an extruded magnesium alloy tested in compression. *Scripta Materialia.* 2011, vol. 65, no. 5, pp. 424–427. ISSN 1359-6462. Available from DOI: `10.1016/j.scriptamat.2011.05.027`.

69. LEJCEK, P. *Grain Boundary Segregation in Metals.* Springer Berlin, 2010. Springer Series in Material Science. ISBN 978-3-642-12504-1. Available from DOI: `10.1007/978-3-642-12505-8`.

70. LEBYODKIN, M. A.; SHASHKOV, I. V.; LEBEDKINA, T. A.; MATHIS, K.; DOBRON, P.; CHMELIK, F. Role of superposition of dislocation avalanches in the statistics of acoustic emission during plastic deformation. *Physical Review E*. 2013, vol. 88, p. 042402. Available from DOI: `10.1103/PhysRevE.88.042402`.

71. ALSTOTT, J.; BULLMORE, E.; PLENZ, D. powerlaw: A Python Package for Analysis of Heavy-Tailed Distributions. *PLoS ONE*. 2014, vol. 9, no. 1, e85777. Available from DOI: `10.1371/journal.pone.0085777`.

72. LOUCHET, F.; WEISS, J.; RICHETON, T. Hall-Petch Law Revisited in Terms of Collective Dislocation Dynamics. *Physical Review Letters*. 2006, vol. 97, p. 075504. Available from DOI: `10.1103/PhysRevLett.97.075504`.

73. HUG, E.; KELLER, C. Size effects and magnetoelastic couplings: a link between Hall–Petch behaviour and coercive field in soft ferromagnetic metals. *Philosophical Magazine*. 2019, vol. 99, no. 11, pp. 1297–1326. Available from DOI: `10.1080/14786435.2019.1580397`.

74. DIETER, G. E. *Mechanical Metallurgy*. McGraw-Hill Book Company, 1988. ISBN 0-07-084187-X.

75. BOHLEN, J.; DOBRON, P.; MEZA GARCIA, E.; CHMELÍK, F.; LUKÁČ, P.; LETZIG, D.; KAINER, K. U. The Effect of Grain Size on the Deformation Behaviour of Magnesium Alloys Investigated by the Acoustic Emission Technique. *Advanced Engineering Materials*. 2006, vol. 8, no. 5, pp. 422–427. Available from DOI: `10.1002/adem.200600023`.

76. WANG, X.; JIANG, L.; LUO, A.; SONG, J.; LIU, Z.; YIN, F.; HAN, Q.; YUE, S.; JONAS, J.J. Deformation of twins in a magnesium alloy under tension at room temperature. *Journal of Alloys and Compounds*. 2014, vol. 594, pp. 44–47. ISSN 0925-8388. Available from DOI: `10.1016/j.jallcom.2014.01.100`.

77. KRAJŇÁK, T.; MINÁRIK, P.; STRÁSKÁ, J.; GUBICZA, J.; MÁTHIS, K.; JANEČEK, M. Influence of the initial state on the microstructure and mechanical properties of AX41 alloy processed by ECAP. *Journal of Materials Science*. 2019, vol. 54, no. 4, pp. 3469–3484. ISSN 1573-4803. Available from DOI: `10.1007/s10853-018-3033-6`.

78. DROZDENKO, D.; BOHLEN, J.; YI, S.; MINÁRIK, P.; CHMELÍK, F.; DOBROŇ, P. Investigating a twinning–detwinning process in wrought Mg alloys by the acoustic emission technique. *Acta Materialia*. 2016, vol. 110, pp. 103–113. ISSN 1359-6454. Available from DOI: `10.1016/j.actamat.2016.03.013`.

79. KNAPEK, M.; MINÁRIK, P.; GREŠ, A.; ZEMKOVÁ, M.; LUKÁČ, F.; BOHLEN, J.; CHMELÍK, F.; KRÁL, R. Spark plasma sintered Mg-4Y-3Nd with exceptional tensile performance. *Materials Science and Engineering: A*. 2022, vol. 849, p. 143481. ISSN 0921-5093. Available from DOI: `10.1016/j.msea.2022.143481`.

List of Figures

List of Tables

List of Abbreviations

AE acoustic emission.

bcc body centered cubic.

BSE back-scattered electrons.

CCDF complementary cumulative distribution function.

CI confidence index.

CRSS critical resolved shear stress.

DSC differential scanning calorimetry.

EBSD electron backscatter diffraction.

fcc face centered cubic.

hcp hexagonal close-packed.

HDT hit definition time.

HLT hit lockout time.

HP Hall-Petch.

IPF inverse pole figure.

KAM kernel average misorientation.

KS Kolmogorov-Smirnov.

MLE maximum likelihood estimators.

SE secondary electrons.

SEM scanning electron microscopy.

SF Schmid factor.

SOC self-organized criticality.

TD thermodilatometry.

UCS ultimate compressive strength.